Computational Particle Mechanics (2025) 12:5507–5527
https://doi.org/10.1007/s40571-025-01086-w

A mixture model for simulating particle-laden flows with the Particle Finite Element Method

Simone Martini[1] · **Massimiliano Cremonesi**[1]

Received: 17 June 2025 / Revised: 29 September 2025 / Accepted: 6 October 2025 / Published online: 2 November 2025

Abstract

Particle-laden flows are fundamental in numerous engineering fields, including environmental hydraulics, sediment transport, and process engineering, where understanding the interaction between fluid and particulate phases is critical for design and prediction. This work presents a novel mixture model for sediment transport within the Particle Finite Element Method (PFEM) framework. The model couples the Navier–Stokes equations for fluid flow with a transport-diffusion equation for sediment concentration, treating sediment as a scalar field rather than discrete particles. This approach enables efficient simulation of fluid–sediment interactions without the computational cost of tracking individual sediment particles and their contacts. PFEM's Lagrangian nature allows the mesh to follow the flow motion, with remeshing strategies implemented to maintain mesh quality during large deformations. The model incorporates both Neumann and Robin boundary conditions for sediment concentration, enabling a realistic representation of sediment deposition and exchange at fluid–bed interfaces. Validation is conducted through two- and three-dimensional test cases, including channel flows, gravity current intrusion with multiple fluids, and sediment deposition in tanks with orifices. Comparisons with experimental data and particle-based simulations demonstrate that the model captures key sediment transport phenomena accurately under low-concentration conditions. The proposed mixture model offers a robust and computationally efficient tool for simulating sediment-laden flows in engineering applications.

Keywords Particle Finite Element Method · Particle-laden flows · Mixture model · Free-surface · Numerical modelling · Sediment transport

1 Introduction

The transport of sediment in natural water bodies such as rivers, lakes, and coastal regions is particularly relevant in hydraulic engineering. Sediment movement leads to erosion and deposition, processes that can significantly alter riverbeds and shorelines over time. These changes affect not only the morphology of the landscape but also the performance and safety of hydraulic structures like dams, where sediment accumulation can reduce energy production and increase the risk of environmental damage. Moreover, sediments typically transport nutrients and contaminants, playing a complex role in ecosystem health.

In parallel, the challenge of protecting land from natural disasters, in particular those involving floods that transport debris such as rocks and sand, is a pressing issue worldwide. These particle-laden flows can inflict damage on infrastructure, agricultural areas, and urban environments, leading to serious social and economic consequences. Consequently, understanding and predicting the behaviour of these flows is essential for both environmental protection and disaster mitigation ([1], [2]).

To address these challenges over the last decades, numerical modelling has emerged as a powerful tool in the study of particle-laden flows. Exploiting computational simulations, valuable insights into the dynamics of sediment transport and the associated environmental processes can be obtained. These models can represent the foundations for more comprehensive analyses of natural disasters and the development of preventive strategies. The primary goal of this work is to

✉ Simone Martini
simone.martini@polimi.it

Massimiliano Cremonesi
massimiliano.cremonesi@polimi.it

[1] Department Civil and Structural Engineering, Politecnico di Milano, Piazza Leonardo da Vinci 32, 20133 Milan, Milan, Italy

develop an efficient and robust numerical framework capable of simulating and analysing large-scale particle-laden flow events. Given the computational complexity of such simulations, particular attention is paid to the balance between model accuracy and efficiency, enabling practical applications in real-world large-scale scenarios.

Particle-laden flows are inherently multiphase systems, consisting of an interaction between a fluid phase and a dispersed solid phase. In the context of sediment transport, the fluid phase is typically water, governed by the Navier–Stokes equations, which describe the conservation of mass and momentum within the flow. Simultaneously, the fluid is in continuous contact with a second, solid phase composed of sediment particles. These sediments can vary in size, concentration, and density, and their movement is strongly coupled with the dynamics of the surrounding fluid.

Accurately capturing the physics of particle-laden flows requires coupling the incompressible Navier–Stokes equations, which describe the fluid phase, with appropriate models for the motion and distribution of the solid phase. In the literature, two main modelling strategies are commonly employed to achieve this coupling. The first treats both phases as continua, while the second represents the fluid as a continuum and the solid phase as a collection of discrete particles.

In the first approach, both the fluid and solid phases are modelled as interpenetrating continua. Each phase is governed by its own set of conservation equations (typically for mass and momentum) solved within the same spatial domain. The interaction between phases is modelled through source terms that represent forces such as drag, lift, and pressure gradients acting between the fluid and the sediment particles. This method is commonly referred to as the Eulerian–Eulerian approach, as both phases are described within an Eulerian framework [3]. However, the approach is more general: the key characteristic is that both phases are treated as continuous media, and in principle, either could be formulated in a Lagrangian frame if required. This approach is particularly well-suited for dense suspensions, where the collective behaviour of the solid phase can be effectively approximated as a continuum.

In contrast, the second approach models the fluid phase as a continuum, governed by the Navier–Stokes equations, while representing the solid phase as a set of discrete particles whose trajectories are tracked individually. The motion of each particle is determined by solving the particle equation of motion, accounting for forces such as fluid-particle interactions, pressure gradients, gravity, and buoyancy. This method is typically referred to as the Eulerian–Lagrangian approach, since the fluid is described in an Eulerian frame and the particles in a Lagrangian one [4]. Nonetheless, the fluid phase could, in principle, also be described in a Lagrangian framework. This approach describes in detail the particle dynamics and is particularly effective for dilute flows, where particle–particle interactions are typically negligible.

An alternative modelling strategy is the use of a mixture model, which couples the Navier–Stokes equations for the fluid phase with an advection–diffusion equation governing the concentration of suspended sediments. In this formulation, the sediment is treated as a scalar field representing its concentration, which directly influences the density and viscosity of the fluid [5]. The result is a continuous mixture where the sediment is not tracked as a separate phase, but rather as a modifying component of the fluid itself. Because the sediment concentration affects the flow field, and the flow in turn influences sediment transport, the system is intrinsically two-way coupled.

This approach is particularly well-suited for modelling suspended sediment transport, under the assumption that the concentration of the solid phase remains relatively low. The primary advantage of the mixture model is its computational efficiency. Unlike the Eulerian–Lagrangian framework, which requires the tracking of individual particle trajectories, or the Eulerian–Eulerian method, which involves solving a full set of conservation equations for both phases, the mixture model introduces only a single scalar transport equation for sediment concentration. This significantly reduces computational cost while still capturing the essential physics of sediment dynamics in dilute suspensions and allows for the application to large-scale engineering problems.

In this work, we propose a mixture model for sediment-laden flows that, unlike standard formulations in the literature, is based on a Lagrangian description of the fluid motion. The main motivation for adopting a Lagrangian framework is its natural ability to track free-surface flows and fluid–fluid interfaces, which is essential in many environmental applications. One of the main challenges in Lagrangian numerical methods, however, is the distortion of the mesh. To address this issue, several strategies have been developed, including the use of background meshes, as in the Material Point Method (MPM), or the adoption of mesh-free techniques such as Smoothed Particle Hydrodynamics (SPH) [6].

In this study, the fluid is modelled using the Particle Finite Element Method (PFEM), a Lagrangian technique that mitigates mesh distortion through continuous remeshing [7, 8]. In PFEM, the fluid domain is discretized with particles that correspond to mesh nodes, and their motion is governed by the Navier–Stokes equations. A key strength of PFEM is its ability to automatically track evolving interfaces, making it particularly well-suited for simulating free-surface flows. However, as the Lagrangian mesh follows the fluid motion, it can undergo severe distortions, leading to the loss of accuracy [9]. To mitigate this issue, a remeshing technique based on Delaunay Tessellation coupled with α-shape scheme is

employed to reconstruct the mesh while preserving node positions.

PFEM has been successfully applied in a wide range of engineering problems, particularly those involving strong evolution of the fluid domains and interface tracking. For instance, it has been used to model fluid–structure interaction (FSI) [10, 11] and to simulate complex mechanical processes such as metal cutting [12], metal additive manufacturing [13–15], and thermomechanical coupling in solid mechanics [16]. In the field of nuclear safety, PFEM has been employed to simulate core melt accidents involving thermally coupled FSI analysis [17]. For erosion and sediment transport, PFEM has been extended to model soil erosion [18] and coupled with the Discrete Element Method (DEM) for particle-sediment transport [19, 20].

Furthermore, PFEM has demonstrated its versatility through the implementation of complex rheological models. For example, [21] applied a Bingham non-Newtonian model to simulate landslides, while [22] used the Oldroyd-B constitutive law to study viscoelastic fluids, such as those involved in 3D concrete printing [23]. Its capacity to handle large-scale problems has also been proven, for example, in the simulation of the Vajont landslide disaster [24], highlighting PFEM potential for complex engineering problems.

In summary, this work presents a numerical framework for modelling sediment transport in free-surface flows based on a mixture model formulated within a Lagrangian description of the fluid motion. The fluid phase is modelled using the Particle Finite Element Method, which offers the capabilities for tracking evolving interfaces and handling large deformations through continuous remeshing. To represent the solid phase, we couple PFEM with an advection–diffusion equation for sediment concentration, creating a computationally efficient mixture model that captures the two-way coupling between fluid flow and suspended sediment. This approach is particularly suited for simulating environmental flows where accurate interface tracking and sediment transport dynamics are essential.

The outline of this article is as follows: Section 2 presents the governing equations of the model and their coupling; Sect. 3 discusses system discretization, numerical challenges, and boundary conditions; Sect. 4 provides an in-depth analysis of PFEM, detailing its features and challenges; Sect. 5 showcases 2D and 3D numerical examples to illustrate model accuracy and applicability; finally, Sect. 6 presents concluding remarks.

2 Governing equations

As already underlined in the previous section, the overall model is structured into two main components: a fluid module and a sediment module. These two modules are coupled, giving rise to a mixture model capable of capturing two-way interactions between fluid flow and sediment transport. The fluid module is based on the Navier–Stokes equations, assuming a Newtonian fluid, which, in the context of this work, is water. The sediment module involves the solution of a mass conservation equation expressed as an advection–diffusion equation for the sediment concentration. The coupling between the two modules is achieved by allowing the sediment concentration to modify the density and viscosity of the fluid, thereby creating a two-way coupled system. This section is organized as follows: first, the fluid and sediment modules are presented individually (Sects. 2.1 and 2.2), followed by a discussion of their coupling (Sect. 2.3).

2.1 Fluid model

Consider a generic bounded, time-dependent domain $\Omega_t \subseteq \mathbb{R}^k$ $(k = 2, 3)$, defined for every $t \in [0, T]$, with $T > 0$. Within this domain, the motion of the fluid is governed by the Navier–Stokes equations for weakly compressible fluids, formulated in a Lagrangian framework:

$$\rho \frac{\mathrm{d}\mathbf{u}}{\mathrm{d}t} = \nabla \cdot \boldsymbol{\sigma} + \rho \mathbf{b} \tag{1}$$

$$\frac{\mathrm{d}p}{\mathrm{d}t} + \kappa \left(\nabla \cdot \mathbf{u}\right) = 0 \tag{2}$$

where $\mathbf{u}$ denotes the fluid velocity, p the pressure field, ρ the fluid density, and κ the bulk modulus. The term $\mathbf{b}(\mathbf{x}, t)$ represents the body forces acting on the fluid. The operator $\frac{\mathrm{d}}{\mathrm{d}t}$ refers to the material (or total) derivative, consistent with the Lagrangian nature of the formulation. The Cauchy stress tensor $\boldsymbol{\sigma}(\mathbf{x}, t)$ is decomposed into an isotropic pressure term and a deviatoric stress component:

$$\boldsymbol{\sigma} = p\boldsymbol{I} + \tau = p\boldsymbol{I} + 2\mu\boldsymbol{\varepsilon}_{\mathrm{dev}} \tag{3}$$

where the deviatoric strain rate tensor $\boldsymbol{\varepsilon}_{\mathrm{dev}}$ is defined as:

$$\boldsymbol{\varepsilon}_{\mathrm{dev}} = \frac{1}{2}\left(\nabla\mathbf{u} + \nabla\mathbf{u}^T\right) - \frac{1}{3}\left(\nabla \cdot \mathbf{u}\right)\boldsymbol{I} \tag{4}$$

The assumption of weak compressibility offers practical advantages in pressure computation, as the pressure field can be recovered directly from the mass conservation Eq. (2). This approach is very close to the incompressible case, since the allowed compressibility is minimal and governed by the magnitude of the bulk modulus κ [8]. Physically, κ quantifies the pressure required to induce a unit volumetric change in the fluid and is typically very high for liquids. For instance, the bulk modulus of water at 20°C is approximately 2.2 GPa [25], ensuring that the term involving $\nabla \cdot \mathbf{u}$ dominates in Eq. (2), effectively fixing the incompressibility of the fluid during the simulation.

2.2 Sediment model

In the same time-dependent domain Ω_t introduced in Sect. 2.1, the sediment transport is modelled through an advection–diffusion equation that governs the evolution of the sediment concentration field. This scalar field represents the local volumetric fraction of sediment within an infinitesimally small control volume, providing a continuum description of the solid phase.

This model is based on the assumption that the sediment can be treated as a continuum, represented by its concentration. Additionally, it is assumed that the sediment is non-cohesive, small grain sizes with respect to the characteristic length scales of the flow, and the local equilibrium approximation. This latter hypothesis implies that once sediment particles start moving, they instantly assume the acceleration of the surrounding fluid [26].

The governing equation for the sediment phase, presented in Eq. (5), is derived from the mass conservation principle applied to the transported solid phase over a representative control volume.

$$\frac{\partial c}{\partial t} + \nabla \cdot \left[\left(\mathbf{u} + w_s\left(c\right) \frac{\mathbf{g}}{|\mathbf{g}|} \right) c \right] = \nabla \cdot \left(\frac{\nu_t}{\sigma_c} \nabla c \right) \tag{5}$$

In Eq. (5), c is the sediment concentration, $w_s\left(\mathbf{x}, t\right)$ is the terminal velocity, $\mathbf{g}$ is the gravity acceleration, ν_t is the sediment diffusivity and σ_c is the Schmidt number defined as the ratio between the kinematic viscosity and the mass diffusivity.

The falling velocity (or terminal velocity) w_s is the speed at which a particle descends only under the influence of gravity. It may vary nonlinearly with sediment concentration, and a widely used empirical relationship is given by [27]:

$$w_s\left(c\right) = w_{s0}\left(1 - c\right)^{\xi} \tag{6}$$

where w_{s0} denotes the terminal velocity of a single particle in clear, still water, and ξ is the hindered settling exponent, which accounts for inter-particle interactions and collective effects in more concentrated suspensions.

Moreover, unless otherwise specified, constant values are assumed for the diffusivity ν_t and the Schmidt number σ_c. Following [28], σ_c will always be considered (if not specified otherwise) equal to 1. Under this assumption, the diffusive term on the right-hand side of Eq. (5) reduces to a Laplacian operator, facilitating its numerical treatment and integration into the overall model.

The advection–diffusion Eq. (5) must be complemented by a suitable set of boundary conditions prescribed on the domain boundary $\partial\Omega_t$. The formulation and implementation of the most relevant types of boundary conditions are discussed in detail in Sect. 3.3.

Given the Lagrangian nature of the adopted framework, it is natural to express the sediment transport equation using the total derivative. Starting from the conservative form, we expand the divergence term to obtain:

$$\frac{\partial c}{\partial t} + \nabla c \cdot \mathbf{u} + \left(\nabla \cdot \mathbf{u}\right) c + \nabla \cdot \left(w_s\left(c\right) \frac{\mathbf{g}}{|\mathbf{g}|} c \right) = \frac{\nu_t}{\sigma_c} \Delta c \tag{7}$$

In (7), the first two terms constitute the material derivative of the concentration, representing its rate of change following the fluid motion. The third term contains the velocity divergence, which vanishes for incompressible flows. However, in this model, we adopt a weakly compressible formulation, where this term is nonzero but typically small. Given that sediment concentration is generally low (as further discussed in Sect. 2.3), this term has a negligible impact and can be safely omitted. The final form of the equation reads:

$$\frac{\mathrm{d}c}{\mathrm{d}t} + \nabla \cdot \left(w_s\left(c\right) \frac{\mathbf{g}}{|\mathbf{g}|} c \right) = \frac{\nu_t}{\sigma_c} \Delta c \tag{8}$$

From (8), it can be understood that sediment dynamics is governed by advection, sedimentation, and diffusion. The material derivative captures transport due to fluid motion, while the sedimentation term models the downward drift of particles under gravity. This drift is influenced by the particle–fluid interactions (detailed discussion in Appendix A). The final term, a Laplacian, represents diffusion of sediment from regions of high-to-low concentration, promoting mixing.

2.3 Coupling—mixture model

In two-phase flow models, the coupling can generally be categorised into two types: one-way and two-way coupling. In one-way coupling, the fluid influences the particles, but the particles do not affect the fluid. This approach is appropriate when the particle concentration is low, such that their collective influence on the fluid motion is negligible. The fluid is thus treated as if it were moving without particles. In contrast, two-way coupling accounts for mutual interaction: the fluid affects the particles, and the particles, in turn, modify the fluid's behaviour. This becomes essential when the particle concentration is sufficiently high to alter the fluid's properties.

In this work, the coupling between sediment and fluid is handled via a mixture model, following the formulation proposed by [5]. Specifically, a two-way coupling is implemented: the computed sediment concentration is used to modify the fluid properties, namely the density and viscosity, effectively transforming the problem into one involving a fluid-sediment mixture. The mixture density is modelled as a linear combination of the densities of the fluid (ρ_f) and the

solid sediment phase (ρ_s), weighted by the local sediment concentration c:

$$\rho(c) = \rho_f(1-c) + \rho_s c \tag{9}$$

Similarly, the dynamic viscosity is adjusted to reflect the presence of suspended particles. The following empirical relation, valid for dilute suspensions, is used:

$$\mu(c) = \mu_f\left(1 + 2.5c + 10.05c^2 + 0.00273e^{16.6c}\right) \tag{10}$$

This expression is based on experimental observations and captures the nonlinear increase in viscosity with sediment concentration [29, 30]. However, it is important to note that this relation is valid primarily for low concentrations (smaller than 0.4) [5]. At higher concentrations, shear-rate-dependent behaviour may emerge [31]. In the present study, the sediment concentration remains within a dilute regime, c smaller than 0.1, ensuring that the assumptions behind this empirical model remain valid.

3 Numerical modelling

The numerical modelling of the proposed mixture model is based on the Finite Element Method (FEM). Both the fluid and sediment transport equations are discretized using a Galerkin FEM formulation. The spatial domain Ω_t is discretized using a finite element mesh $\mathcal{T}_h = \mathcal{T}_h(t)$. Since the formulation adopts a Lagrangian framework, the mesh nodes move with the fluid velocity. This means that the mesh deformation reflects the actual material motion, allowing for an accurate representation of interfaces and free surfaces. The same mesh $\mathcal{T}_h$ is employed to solve both the Navier–Stokes equations and the advection–diffusion equation for sediment concentration, ensuring consistency in the coupling of fluid and sediment dynamics.

3.1 Discretization of the fluid balance equations

Following the standard Galerkin formulation for a 3-dimensional setting ($k = 3$), the spaces of the solution functions $V = [H^1(\Omega_t)]^3$ and $Q = L^2(\Omega_t)$ are introduced. The weak form of the momentum balance is obtained by multiplying Eq. (1) for the generic vector test function $\mathbf{v} \in V_0$ and integrating over the computational domain Ω_t. V_0 is the space of functions belonging to V with a null value on the Dirichlet portion of the boundary. Analogously, the weak form of the mass conservation is achieved by multiplying Eq. (2) for the generic scalar test function $q \in Q$ and integrating over the computational domain Ω_t. The weak form of problem (1)–(2) reads:

$\forall \mathbf{x} \in \Omega_t$ and $\forall t \in [0, T]$, search for $\mathbf{u}(\mathbf{x}, t) \in V$ and $p(\mathbf{x}, t) \in Q$ such that:

$$\begin{aligned}\int_{\Omega_t} \rho \frac{\mathrm{d}\mathbf{u}}{\mathrm{d}t}\mathbf{v}\,\mathrm{d}\Omega_t &= \int_{\Omega_t} (\nabla\cdot\boldsymbol{\sigma})\,\mathbf{v}\,\mathrm{d}\Omega_t + \\ &+ \int_{\Omega_t} \rho\mathbf{b}\mathbf{v}\,\mathrm{d}\Omega_t \qquad \forall \mathbf{v} \in V_0\end{aligned} \tag{11}$$

$$\int_{\Omega_t} \frac{\mathrm{d}p}{\mathrm{d}t} q\,\mathrm{d}\Omega_t + \int_{\Omega_t} \kappa(\nabla\cdot\mathbf{u})\,q\,\mathrm{d}\Omega_t = 0 \qquad \forall q \in Q \tag{12}$$

with $\mathbf{v}(\mathbf{x}, t) \in V_0$ and $q(\mathbf{x}, t) \in Q$ being the test functions. It is important to recall that, due to the application of a mixture model, density and viscosity are dependent on the concentration, i.e. $\rho = \rho(c)$ and $\mu = \mu(c)$, consequently, also the stress depends on the concentration c.

Following a standard Galerkin finite element approach and introducing the spaces $V_h = V \cap X_h^1$ and $Q_h = Q \cap X_h^1$, where X_h^1 is the space of linear test functions built on the grid $\mathcal{T}_h$, the semi-discretized problem in space reads:

$$\mathbf{M}_U \frac{\mathrm{d}\mathbf{U}}{\mathrm{d}t} = \mathbf{F}_{ext} - \mathbf{K}\mathbf{U} + \mathbf{D}^T\mathbf{P} \tag{13}$$

$$\mathbf{M}_P \frac{\mathrm{d}\mathbf{P}}{\mathrm{d}t} + \kappa\mathbf{D}\mathbf{U} = 0 \tag{14}$$

where $\mathbf{U} \in \mathbb{R}^{3N_n}$ and $\mathbf{P} \in \mathbb{R}^{N_n}$ are, respectively, the velocity and pressure vectors and N_n the number of nodes in the mesh. $\mathbf{M}_U \in \mathbb{R}^{3N_n \times 3N_n}$ and $\mathbf{M}_P \in \mathbb{R}^{N_n \times N_n}$ are the mass matrices for velocity and pressure, $\mathbf{K} \in \mathbb{R}^{3N_n \times 3N_n}$ is the viscous matrix and $\mathbf{D} \in \mathbb{R}^{N_n \times 3N_n}$ is the discretization of the divergence operator. Given the set of linear shape functions $\{\phi_i\}_{i=1}^{3N_n}$ for velocity defined on the mesh $\mathcal{T}_h$, the integrals in the momentum balance Eq. (13) are defined as:

$$M_{U,ij} = \int_{\Omega_t} \rho\,\phi_j\phi_i\,d\Omega_t \tag{15}$$

$$F_{ext,i} = \int_{\Omega_t} \rho b_i\phi_i\,d\Omega_t \tag{16}$$

$$K_{ij} = \int_{\Omega_t} 2\mu\left(\boldsymbol{\varepsilon}_{dev}(\phi_j) : \nabla\phi_i\right)\,d\Omega_t \tag{17}$$

Considering $\{\varphi_i\}_{i=1}^{N_n}$ the set of shape functions for pressure, the terms of the mass conservation Eq. (14) are defined as:

$$M_{P,ij} = \int_{\Omega_t} \varphi_j\varphi_i\,d\Omega_t \tag{18}$$

$$D_{ij} = \int_{\Omega_t} (\nabla\cdot\phi_i)\,\varphi_j\,d\Omega_t \tag{19}$$

The use of equal-order interpolation for velocity and pressure violates the LBB (Ladyzhenskaya–Babuška–Brezzi) condition, leading to possible spurious pressure oscillations.

Therefore, the formulation has been stabilized using the Direct Pressure Stabilization (DPS) method [32]. The stabilizing effect is obtained by adding a new term based on the L^2 projection of the linear pressure field onto a constant [32].

Considering the time discretization, a partition of the interval $0 = t^0 < t^1 < ... < t^n < ... < t^m = T$ is introduced, where $t^{n+1} - t^n = \Delta t^n$ $(n = 0, 1, ..., m-1)$ is the time step adopted. In this work, an explicit integration in time with an adaptive time step size is used. The fully discretized system at time t^{n+1} reads:

$$\mathbf{M}_U^n \frac{\mathbf{U}^{n+1} - \mathbf{U}^n}{\Delta t^n} = \mathbf{F}_{ext}^n - \mathbf{F}_{int}^n \tag{20}$$

$$\mathbf{M}_P^{n+1} \frac{\mathbf{P}^{n+1} - \mathbf{P}^n}{\Delta t^n} = -\kappa \mathbf{D}^{n+1} \mathbf{U}^{n+1} \tag{21}$$

where the internal force $\mathbf{F}_{int}^n$ is defined as $\mathbf{F}_{int}^n = -\mathbf{K}^n \mathbf{U}^n + \mathbf{D}^{T,n} \mathbf{P}^n$. Equation (21) is solved in the current configuration of the domain defined by the node positions updated just after the computation of the velocity $\mathbf{u}^{n+1}$, following a linear approximation of the trajectory: $\mathbf{x}^{n+1} = \mathbf{x}^n + \mathbf{u}^{n+1} \Delta t^n$.

Since a coupling is present between the fluid and the sediment, in Eqs. (20) and (21), the influence of the concentration on the fluid operators is considered. Following the explicit approach in the definition of the fluid operators, the concentration field is evaluated at the previous time step $c = c(t^n)$.

The proposed explicit integration scheme is conditionally stable, and so the time step must be limited by the CFL (Courant, Friedrichs, Lewy) condition [33]:

$$\Delta t^n = C_N \min_e \left(\frac{h_e^n}{v_e} \right) \tag{22}$$

where C_N is the Courant number, h_e is the element dimension and v_e is the speed of dilational waves in the fluid. Since the Δt directly depends on the mesh size, special attention must be paid to element distortion. Highly distorted elements tend to have small inscribed sphere radii, which in turn reduce the allowable time integration step, leading to a larger number of time steps and increased computational cost. Due to the Lagrangian formulation, remeshing becomes essential to preserve a reasonable mesh quality and size throughout the simulation.

3.2 Discretization of the sediment mass balance equation

As with the fluid problem, the space discretization of the sediment Eq. (8) is performed using a Galerkin finite element approach. Considering the space $W = H^1(\Omega_t)$, multiplying Eq. (8) by a scalar test function $r(\mathbf{x}, t) \in W_0$ and integrating over Ω_t, the weak form reads: $\forall \mathbf{x} \in \Omega_t$ and $\forall t \in [0, T]$, search for $c(\mathbf{x}, t) \in W$, such that:

$$\begin{aligned} \int_{\Omega_t} \frac{\mathrm{d}c}{\mathrm{d}t} r \, \mathrm{d}\Omega_t + \int_{\Omega_t} \nabla \cdot \left(w_s(c) \frac{\mathbf{g}}{|\mathbf{g}|} c \right) r \, \mathrm{d}\Omega_t \\ = \int_{\Omega_t} \frac{\nu_t}{\sigma_c} \Delta c \, r \, \mathrm{d}\Omega_t \qquad \forall r \in W_0 \end{aligned} \tag{23}$$

where W_0 is the space W with zero Dirichlet boundary conditions, and the term $w_s(c)$ in most cases depends nonlinearly on c. By applying the divergence theorem to the second term in Eq. (23) in order to make the concentration term explicit, and by defining $\mathbf{k} = -\frac{\mathbf{g}}{|\mathbf{g}|}$ as the unit vector in the direction of gravity, the term becomes:

$$\begin{aligned} \nabla \cdot \left(w_s \frac{\mathbf{g}}{|\mathbf{g}|} c \right) &= \nabla \cdot (-w_s \mathbf{k} c) \\ &= -w_{s0} \frac{\partial}{\partial k} \left(c (1-c)^{\xi} \right) \\ &= -w_{s0} \left[\frac{\partial c}{\partial k} (1-c)^{\xi} - \frac{\partial c}{\partial k} c\xi (1-c)^{\xi-1} \right] \\ &= -w_{s0} \frac{\partial c}{\partial k} (1-c)^{\xi} \left[1 - \frac{c\xi}{1-c} \right] \end{aligned} \tag{24}$$

Resulting in the final of the weak formulation of the sediment equation:

$$\begin{aligned} \int_{\Omega_t} \frac{\mathrm{d}c}{\mathrm{d}t} r \, \mathrm{d}\Omega_t - \int_{\Omega_t} \frac{\nu_t}{\sigma_c} \Delta c \, r \, \mathrm{d}\Omega_t + \\ - \int_{\Omega_t} w_{s0} \frac{\partial c}{\partial k} (1-c)^{\xi} \left[1 - \frac{c\xi}{1-c} \right] r \, \mathrm{d}\Omega_t = 0 \\ \forall r \in W_0 \end{aligned} \tag{25}$$

Starting from the weak formulation (25), spatial discretization is introduced. The concentration field, like the fluid variables, is discretized using a linear finite element. On the same mesh $\mathcal{T}_h$ employed for the fluid problem, the concentration $c_h \in W_h = W \cap X_h^1$ is expressed in the discretized setting as:

$$c_h(\mathbf{x}, t) = \sum_{j=1}^{N_n} c_j(t) \varphi_j(\mathbf{x}) \tag{26}$$

using shape functions $\{\varphi_i\}_{i=1}^{N_n}$, where each $\varphi_j \in X_h^1$ for all $j = 1, \ldots, N_n$, leading to the semi-discretized equation in space:

$$\mathbf{M}_C \frac{\mathrm{d}\mathbf{C}}{\mathrm{d}t} = -\mathbf{A}\mathbf{C} + \mathbf{F} \tag{27}$$

$\mathbf{C} \in \mathbb{R}^{N_n}$ is the solution concentration vector, $\mathbf{M}_C \in \mathbb{R}^{N_n \times N_n}$ is the mass matrix, $\mathbf{A} \in \mathbb{R}^{N_n \times N_n}$ is the diffusion matrix for

the sediment and $\mathbf{F} \in \mathbb{R}^{N_n}$ is the forcing due to the deposition effects. The operators described above are defined as:

$$M_{C,ij} = \int_{\Omega_t} \varphi_j \varphi_i \, d\Omega_t \tag{28}$$

$$A_{ij} = \int_{\Omega_t} \frac{\nu_t}{\sigma_c} \nabla\varphi_j \cdot \nabla\varphi_i \, d\Omega_t \tag{29}$$

$$F_i = \int_{\Omega_t} w_{s0} \frac{\partial c}{\partial k} (1-c)^{\xi} \left[1 - \frac{c\xi}{1-c}\right] \varphi_i \, d\Omega_t \tag{30}$$

The expression (30) shows the nonlinear dependence of F_i on concentration c.

Introducing the same partition of the time interval presented in Sect. 3.1 and the same explicit time integration, the discrete problem reads:

$$\mathbf{M}_C^{n+1} \frac{\mathbf{C}^{n+1} - \mathbf{C}^n}{\Delta t^n} = -\mathbf{A}^{n+1}\mathbf{C}^n + \mathbf{F}^n \tag{31}$$

where, consistently with the explicit time integration, the term F_i is evaluated at the previous time step.

The addition of the sediment transport equation introduces a further constraint on the time step, supplementing the CFL condition previously discussed. In particular, a new characteristic velocity associated with sediment diffusion, denoted as v_d, is defined by dividing the effective diffusivity $\frac{\nu_t}{\sigma_c}$ by the characteristic size of a deformed mesh element:

$$v_d = \frac{\nu_t}{\sigma_c h_e^n} \tag{32}$$

Accordingly, the stability condition for the time step is revised to incorporate this additional constraint, yielding:

$$\begin{aligned} \Delta t^n &= C_N \min_e \left(\frac{h_e^n}{v_e}, \frac{h_e^n}{v_d} \right) \\ &= C_N \min_e \left(\frac{h_e^n}{v_e}, \frac{\sigma_c \left(h_e^n\right)^2}{\nu_t} \right) \end{aligned} \tag{33}$$

This updated condition is typically more restrictive than the classical CFL condition (22), as it involves a quadratic dependence on the element size. To ensure stability, the minimum value of Δt^n across all elements is selected.

3.3 Boundary conditions

An appropriate set of boundary conditions must be prescribed to ensure the well-posedness of the full problem. The Lagrangian formulation offers significant advantages when dealing with moving free surfaces, as each point on the surface is naturally tracked by the motion of the particles. However, this same characteristic poses challenges at inflow and outflow boundaries, where the movement of particles causes the boundary location to become undefined over time.

To address this issue, inflow and outflow boundaries are fixed in space and treated using an Eulerian perspective, as proposed in [34]. In these regions, the problem is reformulated within the Arbitrary-Lagrangian–Eulerian (ALE) framework, which allows boundary points to remain stationary while still keeping the Lagrangian description elsewhere in the domain. This hybrid approach enables the imposition of velocity, pressure, and concentration boundary conditions on fixed inflow and outflow surfaces, thereby maintaining the consistency and stability of the overall model (details can be found in [34]).

According to the different problems, the sediment concentration equation must be supplemented with Dirichlet, Neumann, or Robin boundary conditions. The Dirichlet condition is imposed, prescribing the concentration directly at the boundary. However, the implementation of Neumann and Robin conditions requires some additional discussion.

Neumann boundary conditions are typically used to prescribe a flux across the boundary, particularly useful for modelling the behaviour at the bottom boundary of the domain, where sediment tends to settle. In such cases, it is reasonable to assume that no sediment flux crosses the boundary, effectively simulating deposition. As a result, the Neumann condition is applied as a zero-flux boundary on the segment $\Gamma_N \subset \partial\Omega_t$, as expressed in:

$$\frac{\nu_t}{\sigma_c} (\nabla c \cdot \mathbf{n}) = 0 \qquad \forall \mathbf{x} \in \Gamma_N \tag{34}$$

This condition is imposed in the weak formulation (25), integrating by parts the integral of the Laplacian:

$$\begin{aligned} \int_{\Omega_t} \frac{\nu_t}{\sigma_c} \Delta c \, r \, \mathrm{d}\Omega_t = -\int_{\Omega_t} \frac{\nu_t}{\sigma_c} \nabla c \cdot \nabla r \, \mathrm{d}\Omega_t + \\ + \int_{\Gamma_N} \frac{\nu_t}{\sigma_c} (\nabla c \cdot \mathbf{n}) \, r \, d\Gamma = -\int_{\Omega_t} \frac{\nu_t}{\sigma_c} \nabla c \cdot \nabla r \, \mathrm{d}\Omega_t \\ \forall r \in W_0 \end{aligned} \tag{35}$$

As a result, the boundary integral vanishes, and only the domain integral remains, which accounts for the concentration gradient within the interior of the domain.

The Robin condition can be used to model the dynamic behaviour of sediment concentration at the boundaries, allowing the system to evolve towards an equilibrium determined by the soil properties [35]. Let Γ_R denote the portion of the boundary $\partial\Omega_t$ where the Robin condition is applied, and then, the condition can be expressed as:

$$\frac{\nu_t}{\sigma_c} (\nabla c \cdot \mathbf{n}) = \gamma \, (c - c_*) + w_s c \left(\mathbf{n} \cdot \frac{\mathbf{g}}{|\mathbf{g}|} \right) \forall \mathbf{x} \in \Gamma_R \tag{36}$$

where c_* is the equilibrium concentration, γ is a parameter which represents how fast the bottom surface reaches an equilibrium condition and $\mathbf{n}$ is the outwards normal to the boundary surface. The resulting flux through the boundary reflects two contributing effects: the gravitational influence in the vertical direction and the system's natural tendency to reach the equilibrium concentration c_* prescribed on the surface. Supposing no gravitational influence, if the boundary concentration c exceeds the equilibrium c_*, the resulting flux $\nabla c \cdot \mathbf{n}$ is negative, indicating sediment leaving the domain. Conversely, if the concentration is lower than the equilibrium, the flux is positive, representing sediment entering the domain. In both cases, when gravity is taken into account, the total flux is also affected by vertical deposition effects $w_s c \left(\mathbf{n} \cdot \frac{\mathbf{g}}{|\mathbf{g}|}\right)$.

Applying the same procedure used for the Neumann condition to the Laplacian term in expression (25), the boundary integral can be rewritten as:

$$\begin{aligned} &\int_{\Omega_t} \frac{\nu_t}{\sigma_c} \Delta c \; r \; \mathrm{d}\Omega_t = -\int_{\Omega_t} \frac{\nu_t}{\sigma_c} \nabla c \cdot \nabla r \; \mathrm{d}\Omega_t \\ &+ \int_{\Gamma_R} \frac{\nu_t}{\sigma_c} (\nabla c \cdot \mathbf{n}) \, r \; d\Gamma = -\int_{\Omega_t} \frac{\nu_t}{\sigma_c} \nabla c \cdot \nabla r \; \mathrm{d}\Omega_t + \\ &+ \int_{\Gamma_R} \left[\gamma \, (c - c_*) + w_s c \left(\mathbf{n} \cdot \frac{\mathbf{g}}{|\mathbf{g}|} \right) \right] r \; d\Gamma \; \forall r \in W_0 \end{aligned} \tag{37}$$

The terms (35) and (37) replace the right-hand side of the equation (23) corresponding to the weak imposition of the Neumann and Robin boundary conditions, respectively. These terms are incorporated into the weak formulation and discretized following the same approach described in Sects. 2.1 and 2.2.

4 Particle Finite Element Method

As a Lagrangian method, the Particle Finite Element Method (PFEM) is particularly well-suited for simulating free-surface flows, due to its inherent capability to track the motion of moving boundaries. By integrating the governing equations in the current, unknown configuration, PFEM naturally accommodates materials undergoing large displacements. From a numerical standpoint, the Lagrangian formulation eliminates the explicit convective term by embedding it within the material time derivative. This removes one of the main sources of nonlinearity and avoids the need to deal with non-self-adjoint and non-symmetric operators typically present in Eulerian frameworks [8]. Moreover, Eulerian formulations require stabilization techniques, such as SUPG methods, to handle advection-dominated regimes [36].

However, one of the key drawbacks of the Lagrangian approach, in mesh-based solvers, is the issue of mesh distortion. In simulations using explicit time integration, this can become critical. As discussed in Sect. 3.1, the CFL condition (33) must be closely monitored throughout the simulation. Excessive distortion reduces the in-sphere radius of elements, which in turn lowers the maximum allowable time step and significantly increases the number of steps and the computational cost. To mitigate this, a remeshing phase is employed to restore mesh quality and control computational expense. When remeshing is triggered, the element connectivity is discarded and rebuilt from scratch, while node positions are preserved. This process is illustrated in Fig. 1a and b.

Preserving the nodal positions avoids the need to interpolate solution variables between the old and new meshes. This is particularly advantageous when using linear shape functions, since information is stored solely at the element vertices.

Because remeshing can occur multiple times during a simulation, the algorithm must be fast and efficient. The adopted method is based on Delaunay triangulation, which in 2D minimizes the maximum triangle radius and maximizes the minimum angle in the mesh [37]. In 3D, however, this optimal property is lost, and issues such as sliver elements (nearly zero-volume tetrahedra) may arise. To address these challenges in PFEM, various strategies have been proposed, including mesh smoothing operations [38] and the adoption of Virtual Elements [39].

The Delaunay triangulation naturally produces convex domains, which may not accurately represent complex geometries, such as irregular surfaces or boundaries. To overcome this limitation and recover non-convex shapes, the alpha-shape method is employed [40]. After generating the Delaunay mesh, a geometric distortion metric α_e is computed for each element:

$$\alpha_e = \frac{R_e}{h_{mean}} \tag{38}$$

where h_{mean} is a reference characteristic length defined at the beginning of the simulation and R_e denotes the in-sphere radius of the element in 3D (or the circumradius in 2D).

To enforce mesh quality and preserve complex geometrical features, each α_e is evaluated against a threshold $\overline{\alpha}$. If $\alpha_e \leq \overline{\alpha}$, the element is considered excessively distorted and removed from the domain; otherwise, it is retained. This geometrical criterion effectively eliminates poorly shaped elements and facilitates the accurate reconstruction of non-convex boundaries. The value of $\overline{\alpha}$ plays a critical role in influencing the fluid incompressibility during a simulation. An excessively large value may lead to an artificial increase in the total volume, whereas an excessively small value may result in a volume reduction. This issue can be mitigated through various strategies, such as employing an alternative application of the α-shape method based on a level-set

approach [41], or by implementing free-slip boundary conditions [42]. The steps involving remeshing and α-shape are summed up in Fig. 1.

Finally, the PFEM pipeline applied to the mixture model is structured as follows:

1. From the particle nodes, generate the first mesh via the Delaunay triangulation;
2. Apply the α-shape method in order to recover the correct shape of the domain;
3. Solve the discretized momentum balance equation for the mixture with the explicit integration in time, recovering the velocity field $\mathbf{U}^{n+1}$;
4. Update the position of the nodes accordingly to the newly found velocity field: $\mathbf{X}^{n+1} = \mathbf{X}^n + \mathbf{U}^{n+1}\Delta t^n$;
5. Solve the discretized mass balance equation for the mixture using the updated position of the nodes, recovering the pressure $\mathbf{P}^{n+1}$;
6. Solve the discretized equation for the sediment, extracting the sediment concentration field $\mathbf{C}^{n+1}$. Update the density ρ^{n+1} and the viscosity μ^{n+1} of the mixture accordingly to the formulas (9) and (10).
7. Pass to the next time step and check the quality of the mesh: if the mesh is too distorted, perform remeshing by going back to step 1; otherwise go back to step 3.

The same solution scheme is also reported in Algorithm 1.

Algorithm 1 Mixture model algorithm

while $t < T$ **do**
  if Mesh distortion $\geq$ threshold **then**
    Do remeshing + α-shape
  end if
  Solve the mixture momentum balance Eq. (20), recovering the velocity $\mathbf{U}^{n+1}$;
  Update the position of the particles: $\mathbf{x}^{n+1} = \mathbf{x}^n + \mathbf{U}^{n+1}\Delta t^n$;
  Solve the mixture mass balance Eq. (21), recovering the pressure $\mathbf{P}^{n+1}$;
  Solve the sediment mass balance Eq. (31), recovering the pressure $\mathbf{C}^{n+1}$;
  Update the nodal density ρ^{n+1} and viscosity μ^{n+1} following the relations 9 and 10;
end while

5 Examples

The proposed framework is first assessed through simple benchmark cases to validate and verify the solution of the sediment transport equation within the flow (Sect. 5.1). Subsequently, a 2D test case is carried out to compare the numerical results with available experimental data (Sect. 5.2). Finally, a complex 3D deposition scenario involving a perforated tank is analysed to demonstrate the model's capabilities in more realistic and challenging conditions (Sect. 5.3).

5.1 2D verification of the sediment equation

In this section, a series of tests are presented to validate the accurate resolution of the sediment transport equation. The verification is performed by comparing the PFEM results against two semi-analytical solutions for one-way coupled problems. In both test cases, a dimensionless formulation is adopted using the following variables:

$$C = \frac{c}{c_a} \quad C_* = \frac{c_*}{c_a} \quad X = \frac{x}{h}$$
$$Y = \frac{y}{h} \quad K = \frac{\frac{\nu_t}{\sigma_c}}{hu_*} \quad T = \frac{tu_*}{h}$$
$$B = \frac{\gamma}{u_*} \quad U_j = \frac{u_j}{u_*} \quad V_s = \frac{w_s}{u_*}$$

where c_a is a reference concentration, h is the characteristic length and u_* is the friction velocity. The friction velocity is defined from the shear stress at the wall τ_w:

$$u_* = \sqrt{\frac{\tau_w}{\rho}} \tag{39}$$

It is commonly employed in turbulence theory as a characteristic velocity scale for fluctuations in the near-wall region, where a boundary layer may occur. In river hydraulics, this law is applied to quantify the potential magnitude of bed erosion, under the assumption of a logarithmic velocity profile [43].

5.1.1 Sediment deposition

As a first verification case, a simulation of sediment deposition in a free-surface channel flow of height h is presented. The scenario involves a still fluid, with sediment concentration evolving due to gravity and boundary effects. The sediment transport is driven by the lack of equilibrium at the bottom boundary, enforced through a Robin boundary condition, which induces a flux into the domain. Specifically, the initial concentration C within the domain differs from the prescribed equilibrium concentration C_*. This is a time-dependent problem, and the numerical results are compared with those obtained in [44].

The simulation setup is illustrated in Fig. 2, which serves as the reference configuration. The semi-analytical solution used for comparison is derived from the resolution of Eq.

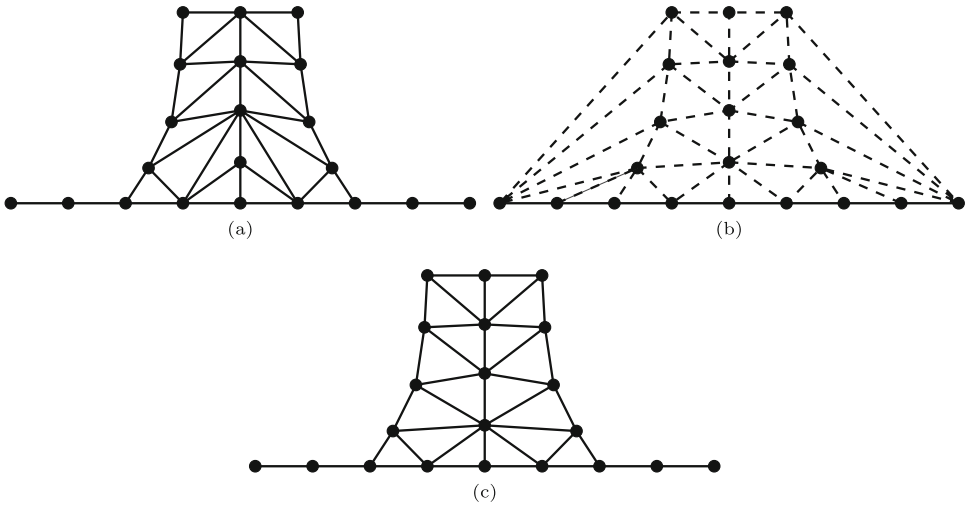

Fig. 1 Remeshing and α-shape steps: from a distorted mesh (1a), the elements are eliminated and a new convex grid is recreated (1b), eliminating the elements that do not belong to the real domain through the α-shape method (1c)

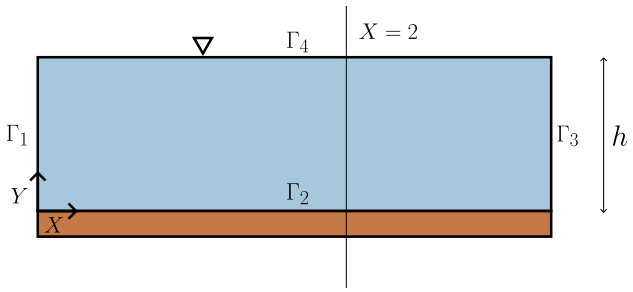

Fig. 2 Initial geometry of the 2D deposition simulation. The blue colour indicates the fluid-sediment domain, while the sand colour indicates the bed domain

(40), as presented in [35].

$$\frac{\partial C}{\partial T} = V_0 \frac{\partial C}{\partial Y} + K \frac{\partial^2 C}{\partial Y^2} \tag{40}$$

The corresponding boundary conditions applied in this verification case are summarized in (41).

$$BC : \begin{cases} C = 1 & \text{on } \Gamma_1 \\ K \frac{\partial C}{\partial Y} + V_0 C = B\,(C - C_*) & \text{on } \Gamma_2 \\ \nabla C \cdot \mathbf{n} = 0 & \text{on } \Gamma_3 \\ K \frac{\partial C}{\partial Y} + V_0 C = 0 & \text{on } \Gamma_4 \end{cases} \tag{41}$$

On Γ_1, the concentration is prescribed as 1, corresponding to the reference value c_a. At the bottom boundary Γ_2, the equilibrium concentration C_* is imposed through a Robin boundary condition. On Γ_3, an outflow condition is enforced by setting the normal derivative of the concentration to zero. Finally, on the free surface Γ_4, no equilibrium concentration is prescribed; however, a flux may occur due to sediment settling under gravity at the terminal velocity V_0.

The initial condition for the dimensionless concentration is $C = 1$ uniformly throughout the domain. The fluid is assumed to be water, with $\rho_f = 1000 \frac{\text{kg}}{\text{m}^3}$ and $\mu_f = 0.001\text{Pa}\cdot\text{s}$. Regarding the sediment parameters, the dimensionless diffusivity coefficient is $K = 0.35$, and the dimensionless settling velocity is $V_0 = 1$. The hindered settling exponent is set to $\xi = 0$, implying a constant settling velocity w_s, independent on the concentration. For the implementation of the Robin boundary condition, the dimensionless equilibrium concentration is set to $C_* = 2$, and the dimensionless parameter governing the exchange rate at the boundary is $B = 1$.

The result in Fig. 3 shows the comparison of the PFEM simulation with the semi-analytical solution. Starting from the initial profile indicated by the dashed line, the imposed equilibrium concentration $C = 2$ at the bottom boundary generates an inward flux of sediment. This flux causes the concentration near the boundary to temporarily exceed the equilibrium value, as illustrated by the profile at $t = 0.4$s. Subsequently, the concentration begins to stabilize and approach the equilibrium state. This overshooting behaviour was also observed experimentally by [45]. After some time, the concentration at the bottom will asymptotically settle towards the equilibrium $C_* = 2$. In Fig. 3d is shown the steady-state profile reached at $t = 5s$.

Overall, a good agreement is achieved between the numerical and semi-analytical results, confirming the accurate resolution of the sediment transport equation under these specific conditions.

5.1.2 Sediment transport in free-surface channel flow

As a second verification case for the sediment equation, the problem proposed by [46] is considered. This case involves a free-surface channel flow with moving fluid. To handle the inlet and outlet boundary conditions, the nodes at these interfaces are fixed in space, following the approach described in Sect. 3.3. The velocity profile imposed at the

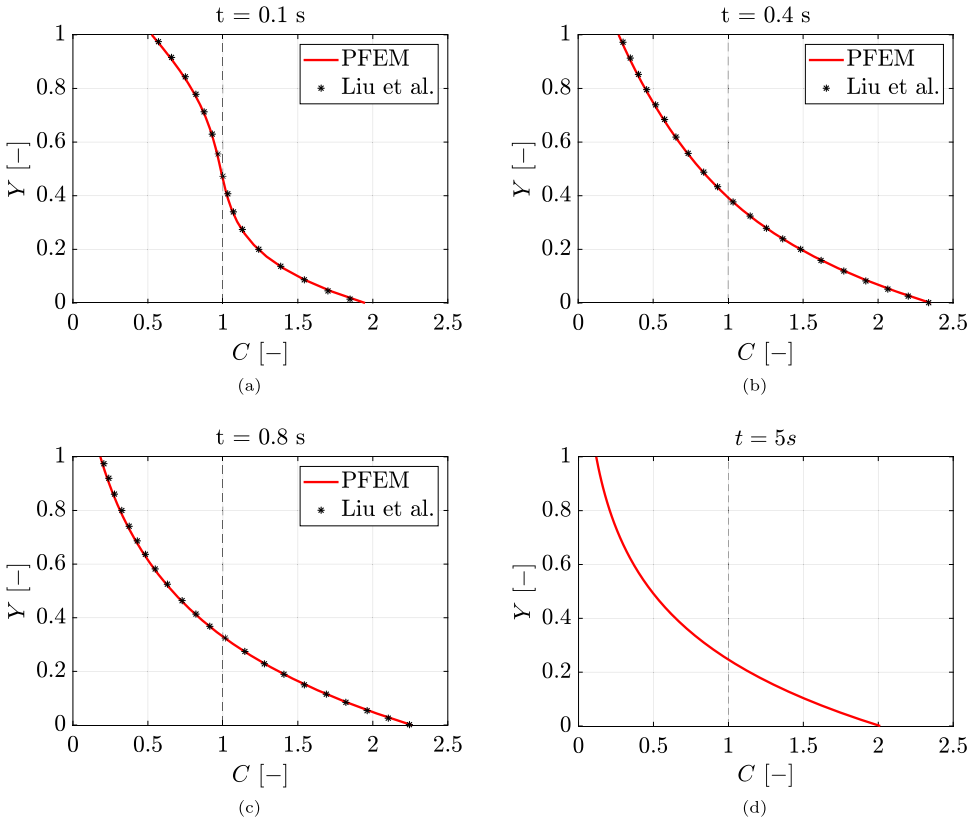

Fig. 3 Concentration plot versus Y at $X = 2$ for $t = 0.1\ s$ (3a), $t = 0.4\ s$ (3b), $t = 0.8\ s$ (3c). Comparison with the results of [44]. In Fig. 3d , the steady-state concentration profile is displayed at $t = 5s$

inlet is $U_x = 0.1691 ln\left(\frac{Y}{0.001}\right)$, and it is maintained constant throughout the simulation within the domain.

The fluid is water with $\rho_f = 1000 \frac{kg}{m^3}$ and $\mu_f = 0.001 Pa \cdot s$. The problem involves solving Eq. (42) under steady-state conditions.

$$U_x \frac{\partial C}{\partial X} - V_0 \frac{\partial}{\partial Y}\left[C\left(1 - c_a C\right)^{\xi}\right] = \frac{\partial}{\partial Y}\left(K\left(Y\right)\frac{\partial C}{\partial Y}\right) \quad (42)$$

The initial configuration is illustrated in Fig. 4, while the boundary conditions are summarized in (43).

$$BC: \begin{cases} C = 0 & \text{on } \Gamma_1 \\ K\frac{\partial C}{\partial Y} + V_0 C = B\left(C - C_*\right) & \text{on } \Gamma_2 \\ \nabla C \cdot \mathbf{n} = 0 & \text{on } \Gamma_3 \\ K\frac{\partial C}{\partial Y} + V_0 C = 0 & \text{on } \Gamma_4 \end{cases} \quad (43)$$

On Γ_1, the concentration is prescribed as 0. At the bottom boundary Γ_2, the equilibrium concentration C_* is imposed via a Robin boundary condition. On Γ_3, an outflow condition is applied by setting the normal derivative of the concentration to zero. Finally, on the free surface Γ_4, no equilibrium concentration is prescribed; nevertheless, a flux may occur due to sediment settling under gravity with the terminal velocity V_0.

The hindered settling exponent is set to $\xi = 4$ and the dimensionless sediment diffusivity varies with the Y coordinate according to the quadratic relation $K = K\left(Y\right) = \frac{\kappa_{vk}}{\sigma_c} Y\left(1 - Y\right)$ with $\kappa_{vk} = 0.41$ the Von-Karman constant. This spatial variability of the diffusivity along the Y-direction introduces an additional term in the governing equation, since the initial assumption of a constant $\frac{\nu_t}{\sigma_c}$ ratio made in Sect. 2.2 no longer holds. The sediment transport parameters used are $V_s = 0.2$, $B = 0.2$ and $C_* = 1$.

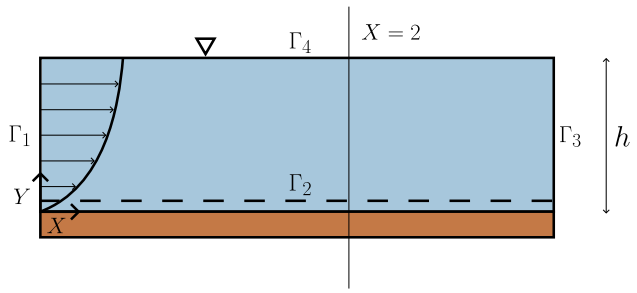

Fig. 4 Initial geometry of the 2D free-surface channel flow simulation. The blue colour indicates the fluid-sediment domain, while the sand colour indicates the bed domain

To investigate the steady-state solution, the time-dependent problem is solved until the concentration profile stabilizes and becomes time-invariant. Figure 5 presents the resulting concentration profiles along the vertical direction Y at $X = 2$ for different reference concentration values: $c_a = 0.02$ (Fig. 5a), $c_a = 0.05$ (Fig. 5b) and $c_a = 0.1$ (Fig. 5c).

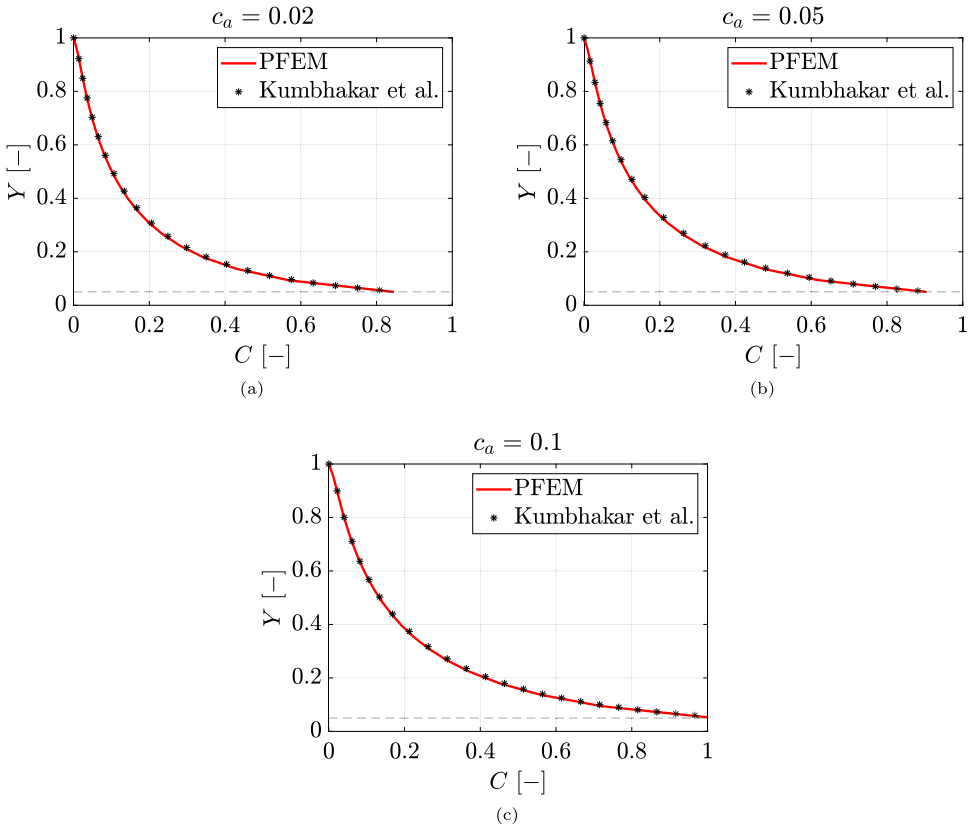

Fig. 5 Concentration along $Y = \frac{y}{h}$ plot at $X = 2$ considering: $c_a = 0.02$, $c_a = 0.05$, $c_a = 0.1$. Comparison with the results of [46]

The initial concentration is set to zero throughout the entire domain. Over time, the concentration increases due to the influence of the Robin boundary condition applied at the bottom, which drives the solution towards an equilibrium value of 1 at the bed. A fluid–soil interface layer is defined at the reference level $Y = 0.05$, where the Robin condition is enforced, as described in [47]. Close to this reference level, the concentration rises sharply, while near the free surface it remains negligible, since a zero-flux Neumann boundary condition is imposed there. As in the previous case, the comparison with the semi-analytical solution presented by [46] demonstrates excellent agreement.

5.2 2D validation of the mixture model

In this section, the mixture model is validated against an experimental setup involving the intrusion of gravity currents. This type of experiment has been conducted under various configurations (see, for example, [48], [49]) and has also been numerically simulated in [50]. It illustrates the dynamics of mixing between three fluids with differing densities. Specifically, the configuration considered here is based on the experiment described in [49], and the initial geometry is depicted in Fig. 6.

Three fluids with different densities are considered in this setup. Two of them are initially arranged in horizontal layers,

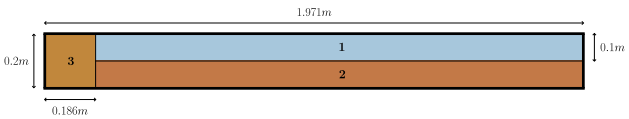

Fig. 6 Initial geometry of the 2D simulation representing the mixing of 3 fluids. As shown in Table 1, fluid 1 in blue corresponds to clear water, while fluids 2 and 3, depicted in two shades of sand, contain sediment at different concentrations

Table 1 Values of density and concentration for each fluid

Fluid n°	Density $[\frac{kg}{m^3}]$	Concentration [−]
1	$\rho_1 = 1000$	$c = 0$
2	$\rho_2 = 1020$	$c = 0.012122$
3	$\rho_3 = 1010$	$c = 0.006061$

while the third fluid, with an intermediate density, is confined to the left side of the domain. To retain this fluid prior to the start of the simulation, a gate is positioned between the regions. The starting mesh consists of 35883 nodes and 70411 elements, while the average time integration step of the simulation is $1.23 \times 10^{-6} s$.

The simulation begins by removing the gate, allowing the fluids to interact and mix. In the framework of the mixture model, different densities imply different concentrations of sediment. So, for each fluid, a concentration of sediment is

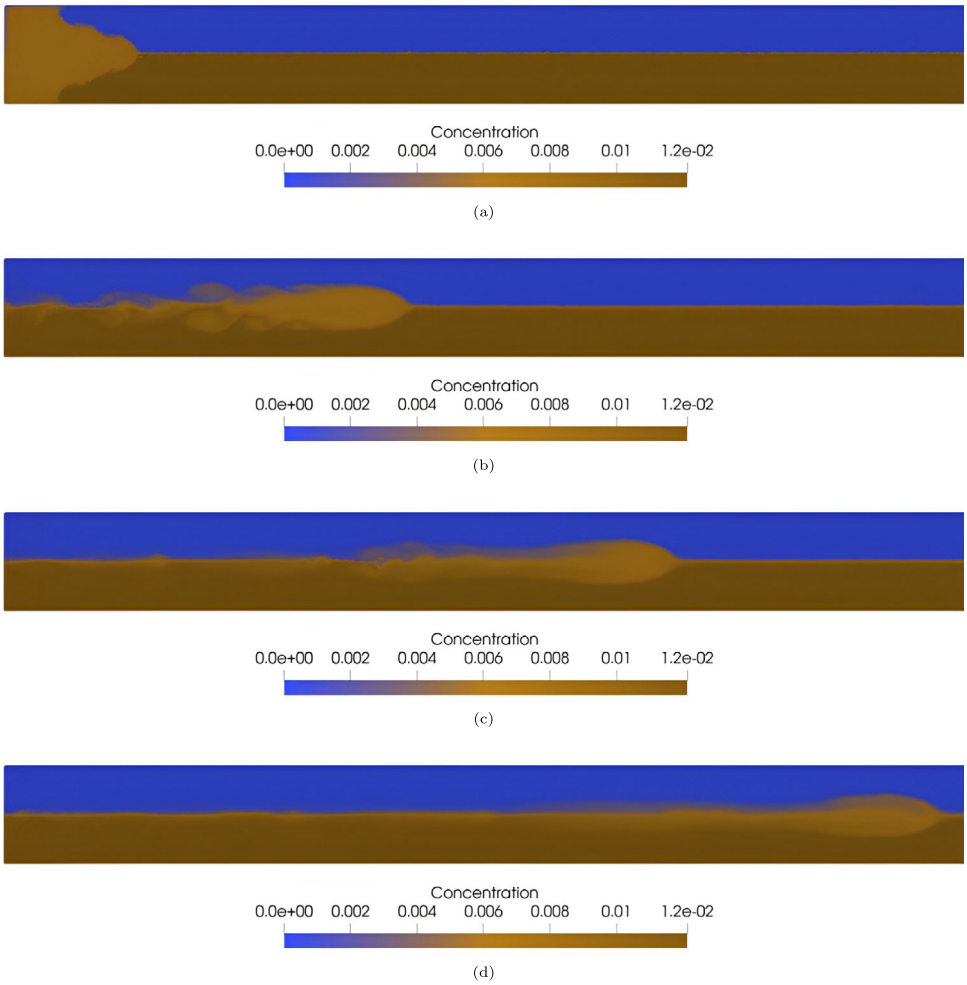

Fig. 7 Concentration field at $t = 2s$ (7a), $t = 14s$ (7b), $t = 26s$ (7c) and $t = 38s$ (7d)

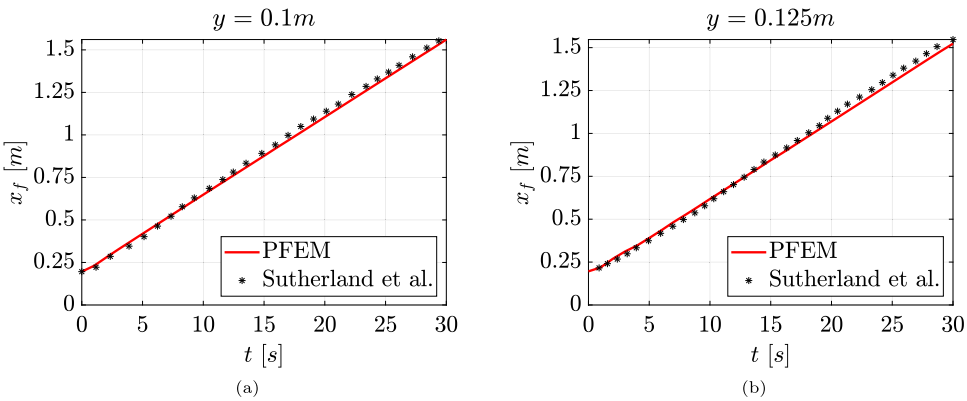

Fig. 8 Perturbation front over time at $y = 0.1m$ and $y = 0.125m$. Comparison with the experimental results of [49]

computed to reach the desired density. The corresponding values of density and sediment initial concentration are summarized in Table 1.

The entire channel has a length of $L = 1.971$m and a total height of $2h = 0.2$m, where h denotes the height of each fluid layer. The length of the fluid initially confined on the left side, referred to as the *lock-length*, is $l = 0.186$m. The sediment density is set to $\rho_s = 2650\frac{\text{kg}}{\text{m}^3}$, while the fluid density and viscosity are $\rho_f = 1000\frac{\text{kg}}{\text{m}^3}$ and $\mu_f = 0.001$Pa·s, respectively. Since the dynamics of the problem are driven solely by density differences, the turbulent diffusivity and settling velocity are both set to zero: $\nu_t = 0\frac{\text{m}^2}{\text{s}}$ and $w_s = 0\frac{\text{m}}{\text{s}}$.

Figure 7 presents four snapshots at different time instants, illustrating the evolution of the flow. Since the fluid initially in the lock has intermediate density, it tends to intrude between the upper and lower layers, generating a perturbation wave

that propagates from left to right. As the simulation progresses, mixing between the three interacting fluid domains leads to a gradual loss of sharp interface definition. This continuous mixing dilutes the local sediment concentration, causing the intrusive current to progressively lose its initial density. Consequently, by the end of the simulation, the wave front becomes more diffuse and less distinguishable compared to the earlier time frames.

This test case demonstrates the method's capability to capture complex interactions between fluids of varying densities, governed by sediment concentration differences. The comparison with the experiment results is provided in Fig. 8 where the horizontal position of the intrusion front x_f is tracked over time at two vertical locations: $y = 0.1$m (8a) and $y = 0.125$m (8b). To extract this front location from the simulation, a perturbation velocity is defined. Based on the experimental observations, the perturbation propagates with approximately constant horizontal velocity. This velocity is used to identify mesh nodes associated with the wave front. The front position x_f is then defined as the maximum x-coordinate among all points whose x-velocity is larger than or equal to the reference wave velocity. The results demonstrate good agreement between the experimental observations and the numerical results, even in this complex test case.

5.3 3D simulation of a sediment deposit inside a holed tank

In this section, a three-dimensional example is presented to demonstrate the capability of the proposed mixture model in addressing realistic engineering problems. The results are compared against a reference simulation performed using the PFEM-DEM (Discrete Element Method) approach from Franci et al. [20], which directly tracks individual particles. This comparison highlights the differences between the mixture-based continuum modelling and a more direct particle-resolved simulation.

The computational domain consists of a cubic tank with side length $L = 1m$, featuring a circular hole at the centre of the bottom surface. A total of 2552 sediment physical particles, all with identical shape and size, are initially placed at rest inside the tank, forming a cylindrical column of sediment with diameter $D = 0.8m$ and height $H = 0.1m$. The initial configuration of the domain is illustrated in Fig. 9.

The fluid is water with $\rho_f = 1000\frac{kg}{m^3}$ and $\mu_f = 0.001 Pa\cdot s$. Two simulations are presented, with different sediment densities of $\rho_s = 1500\frac{kg}{m^3}$ and $\rho_s = 1125\frac{kg}{m^3}$. The hindered settling exponent has been taken as $\xi = 5$.

Since the comparison is made with a particle-based approach, the values of the parameters w_s and ν_t are not directly available. In this context, diffusive effects due to concentration gradients are negligible (as the gradient is very small), so $\nu_t = 0\,\frac{m^2}{s}$. However, the terminal settling velocity w_s is essential and must be determined. This is done by analysing the problem of a particle settling under gravity in a still fluid. The detailed procedure for calculating and validating the terminal velocity is provided in Appendix A. The computed settling velocities in clear water for the two sediment densities are, respectively, $w_{s0} = 0.2746\,\frac{m}{s}$ and $w_{s0} = 0.1221\,\frac{m}{s}$. The particle diameter used in the simulations is $d_m = 0.005\,m$.

Regarding the boundary conditions, a Neumann condition $\nabla c\cdot\mathbf{n} = 0$ is imposed on the bottom surface of the tank, while Dirichlet conditions $c = 0$ are applied on all other container boundaries. To determine the initial concentration inside the cylinder, the total volume occupied by the particles, $V_{p,i}$, is calculated and then divided by the volume of the confining cylinder, V_c (represented by the brown disc in Fig. 9a), as

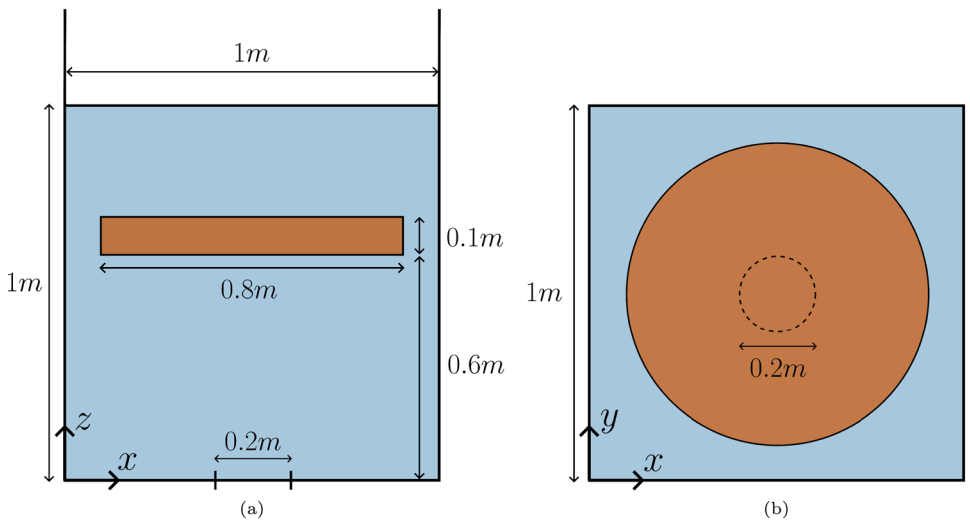

Fig. 9 Starting geometry of the 3D simulation of sediment deposition inside a tank with a hole: 9a lateral view, 9b upper view. A disc of sediment, coloured in brown, is placed inside the tank filled with clear water. An outlet hole is located at the centre of the bottom surface

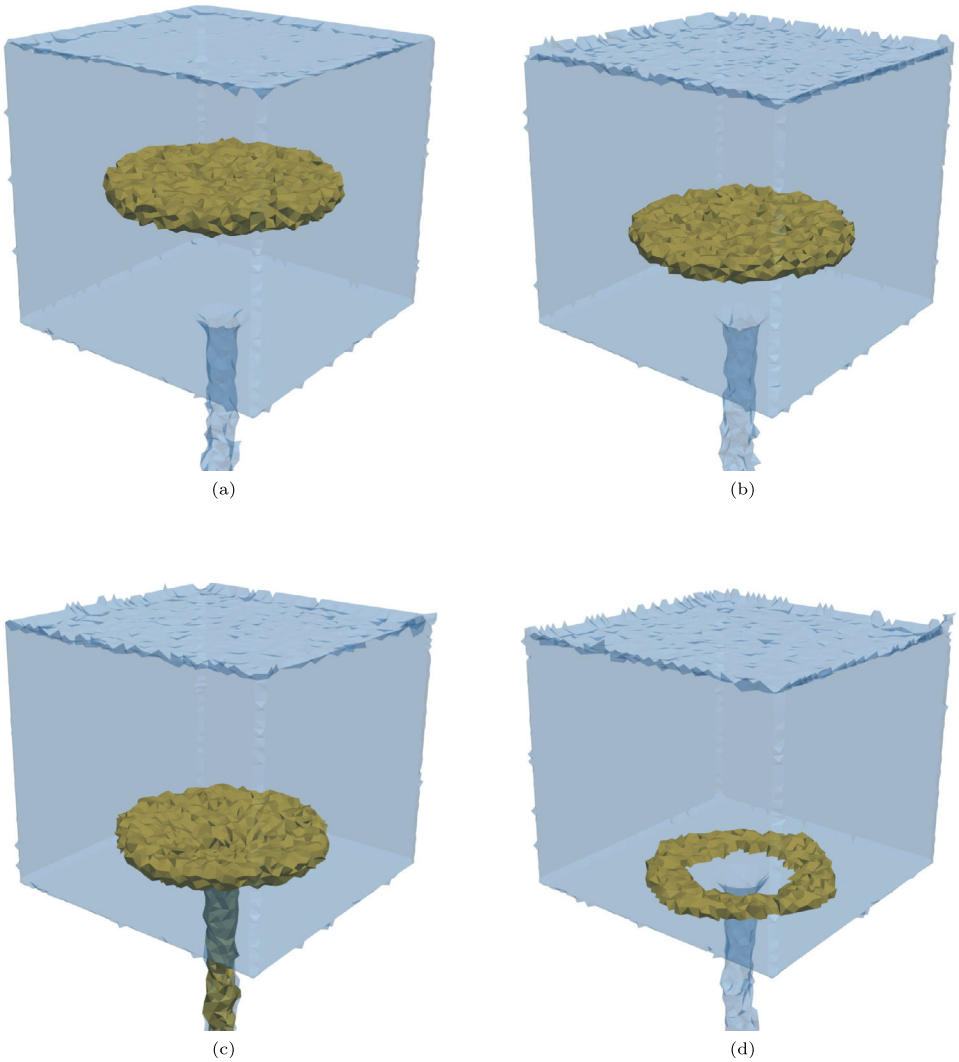

Fig. 10 Cloud deposition at 4 different frames: $t = 0.5s$ (10a), $t = 1s$ (10b), $t = 1.5s$ (10c) and $t = 2s$ (10d), $\rho_s = 1500 \frac{kg}{m^3}$

detailed in Eq. (44).

$$c_0 = \frac{\sum_i V_{p,i}}{V_c} = 0.003322 \tag{44}$$

The resulting initial concentration is $c_0 = 0.003322$, which is well below the maximum limit allowed by the mixture model. The starting mesh has 54472 nodes and 301088 elements. The mean time step of the explicit scheme is $\Delta t_{mean} = 4.2 \times 10^{-6} s$.

When the simulation begins, water flows out through the hole, causing the fluid volume inside the tank to decrease. As the fluid passes through the orifice, the velocity significantly increases, particularly near the centre of the cube. Consequently, the sediment cloud is dragged downward, aided by its weight. Upon reaching the hole, the particles form a funnel shape due to the higher velocity of the mixture at the centre. For the case of higher sediment density, the increased weight causes the cloud to reach the exit hole more rapidly.

For $\rho_s = 1500 \frac{kg}{m^3}$, the sediment completely clears from the tank in just 2 s, leaving only a few deposits on the bottom surface. This behaviour is enabled by the Neumann boundary condition imposed on the bottom surface. All of these comments are supported by the images in Fig. 10.

In the case of $\rho_s = 1125 \frac{kg}{m^3}$, similar dynamics occur, but the sediment's lower density results in a reduced gravitational effect. Consequently, the sediment cloud takes longer to evacuate the container. Indeed, as shown in the last snapshot of Fig. 11 at $t = 3.5\,s$, sediment is no longer flowing through the orifice.

In both cases, the free surface height was verified to remain unaffected by the presence of sediment, as the internal concentration is negligible.

Since in this particular example the sediment equation is advection-dominated, a stabilization has been introduced. This has been achieved by inserting some fictitious diffusion along the direction of advection, which is the z-direction [33]. In order to make a fair comparison to the DEM approach, a

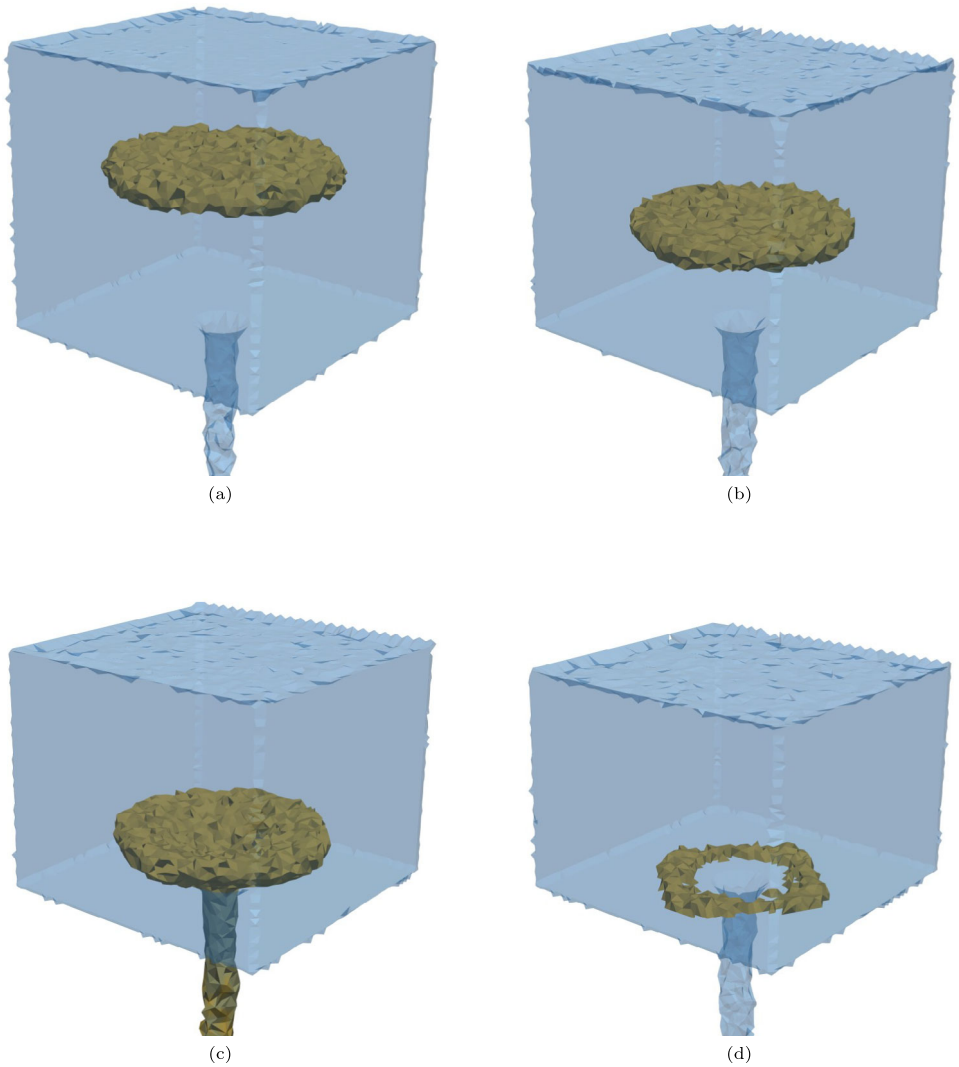

Fig. 11 Cloud deposition at 4 different frames: $t = 0.5s$ (11a), $t = 1.5s$ (11b), $t = 2.5s$ (11c) and $t = 3.5s$ (11d), $\rho_s = 1125 \frac{kg}{m^3}$

threshold concentration has been defined, accounting also for the diffusion effect of the mixture model. In Figs. 12 and 13, the particles highlighted are the ones with concentration greater to the threshold, comparing this cloud with the one coming from [20].

In these figures, the container is cut in the middle along the x-z plane, and the DEM results from [20] are presented as lines outlining the particle cloud. The two approaches show good agreement, with minor differences in the final frame: some particles in the DEM simulation are still exiting the container, while the mixture model shows no sediment flow at this stage. This discrepancy arises from the thresholding: the mixture model excludes concentrations below the threshold, thus missing isolated particles with very low concentration that the DEM method can capture.

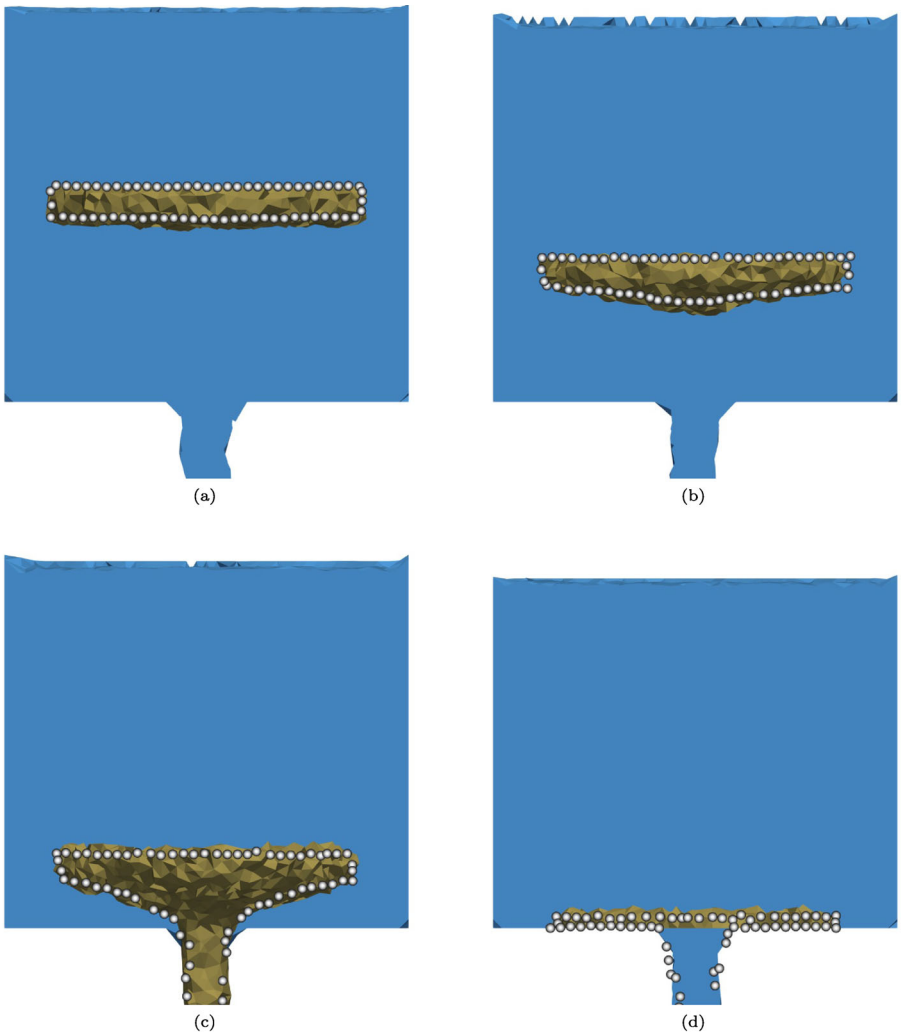

Fig. 12 Cloud plot in the middle $x - z$ section of the tank at $t = 0.5s$ (12a), $t = 1s$ (12b), $t = 1.5s$ (12c) and $t = 2s$ (12d), $\rho_s = 1500 \frac{kg}{m^3}$. Comparison with the results of [20]

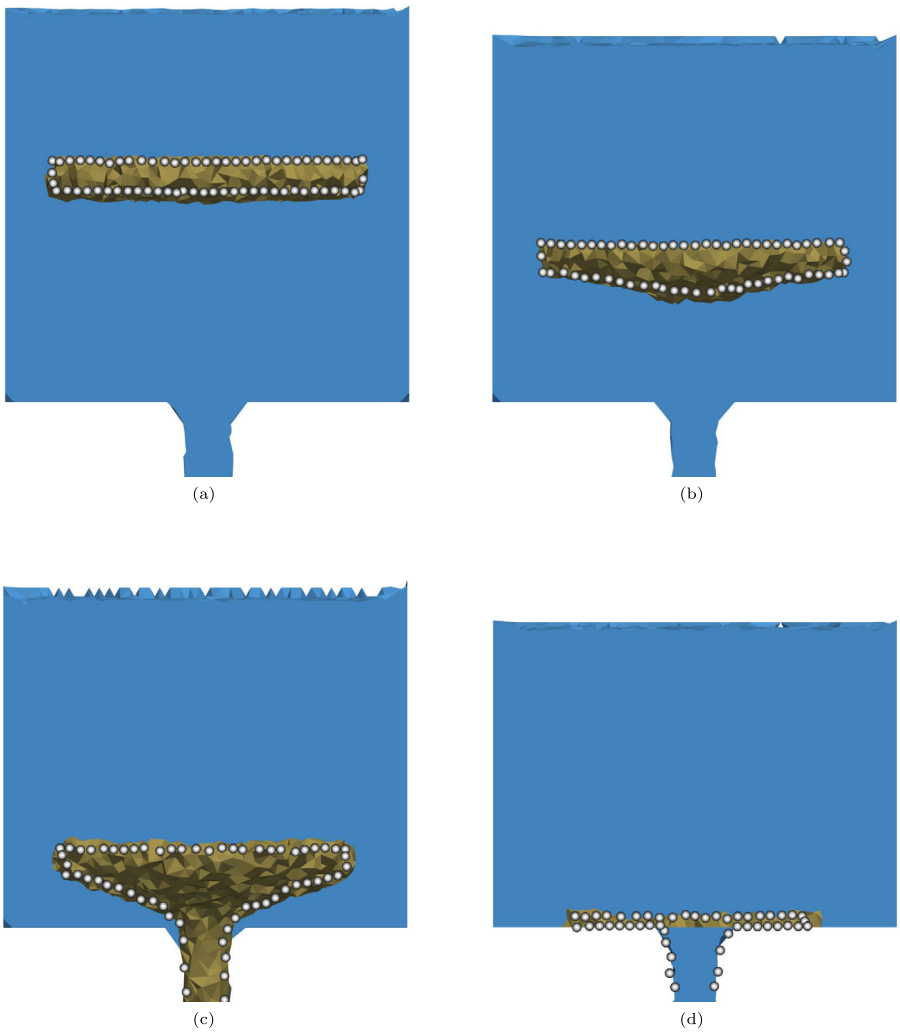

Fig. 13 Cloud plot in the middle $x - z$ section of the tank at $t = 0.5s$ (13a), $t = 1.5s$ (13b), $t = 2.5s$ (13c) and $t = 3.5s$ (13d), $\rho_s = 1125 \frac{kg}{m^3}$. Comparison with the results of [20]

6 Conclusions

In this work, a new numerical methodology has been proposed for modelling sediment transport within the Particle Finite Element Method (PFEM) framework. The approach is based on a two-phase flow formulation, where sediment and fluid are treated as a mixture. A dedicated transport equation for the sediment concentration c has been introduced, with its influence directly embedded into the Navier–Stokes equations through variable fluid density and viscosity.

The formulation has been implemented using linear finite elements and an explicit time integration scheme. Special attention has been given to the correct treatment of boundary conditions for the sediment concentration, including both Neumann and Robin types. These boundary conditions enable the simulation of realistic interactions such as particle deposition and fluid–bed interface dynamics. In particular, Neumann conditions capture zero-flux behaviour or deposition on impermeable surfaces, while Robin conditions allow for modelling equilibrium exchange with a sediment bed layer.

The proposed method has been verified and validated through a series of two-dimensional and three-dimensional benchmark cases. These include steady-state and transient sediment-laden channel flows, gravity current intrusions involving three fluids with different densities, and realistic 3D sediment deposition within a tank with an outlet. In all cases, the model demonstrated good agreement with analytical solutions, experimental data, or alternative numerical approaches (such as PFEM-DEM).

Overall, the results indicate that the proposed mixture-based approach is a flexible and effective tool for simulating sediment transport phenomena in free-surface and enclosed flow problems using PFEM. While the current formulation is effective for low-to-moderate sediment concentrations, some limitations remain for highly concentrated flows. These challenges offer opportunities for future work, such as extending the model to capture particle–particle interactions, non-

Newtonian effects, or extending the approach to highly concentrated flows.

Appendix A Terminal velocity computation

To compute the terminal velocity used in Section 5.3, a benchmark problem involving a single particle falling freely in a still fluid was solved. This test case is widely recognized as a standard validation scenario for particle transport models [51]. It tracks the velocity reached by the particle when forces of weight, buoyancy and drag are considered. In particular, the governing equation to solve is the particle equation of motion

$$m_p \frac{\mathrm{d}\mathbf{v}}{\mathrm{d}t} = \mathbf{F}_d + \mathbf{F}_b + \mathbf{F}_g \tag{A1}$$

where m_p is the mass of the particle, $\mathbf{v}$ is the velocity of the particle, $\mathbf{F}_d$ is the drag force, $\mathbf{F}_b$ is the buoyancy force and $\mathbf{F}_g$ is the gravity force.

The particle is released inside a container filled with a still fluid, and its vertical velocity is computed over time until it stabilizes at a constant value. This steady-state value is defined as the terminal velocity of the particle.

The governing equation has been implemented within the PFEM framework and validated against an analytical solution provided by [52], assuming a Stokesian flow regime in which the drag force depends linearly on the particle velocity. The expression for the drag force and the corresponding analytical solution for the particle velocity are given in Eqs. (A2) and (A3), respectively.

$$\mathbf{F}_d = 3\pi\mu_f d_p \mathbf{v} \tag{A2}$$

$$v_z = \frac{g V_p(\rho_p - \rho_f)}{3\pi\mu_f d_p}\left(1 - e^{\frac{-3\pi\mu_f d_p t}{V_p \rho_p}}\right) \tag{A3}$$

where μ_f and ρ_f are the fluid viscosity and density, while d_p, V_p, and ρ_p are, respectively, the diameter, volume and density of the particle. For this particular example, $\rho_p = 2500\frac{kg}{m^3}$, $d_p = 0.0001m$, $\rho_f = 1000\frac{kg}{m^3}$, $\mu_f = 0.001Pa \cdot s$ and the particle has a spherical shape. A comparison between the PFEM simulation results and the analytical solution is shown in Fig. 14, demonstrating excellent agreement and validating the accuracy of the terminal velocity computation.

Given the agreement between the PFEM simulation and the analytical solution under Stokesian flow conditions, the model can now be confidently used to compute the terminal velocities required in the problem described in Section 5.3. For this purpose, a different drag formulation has been employed, where the drag force depends quadratically on the relative velocity between the fluid and the particle. This quadratic drag law is more appropriate for higher Reynolds

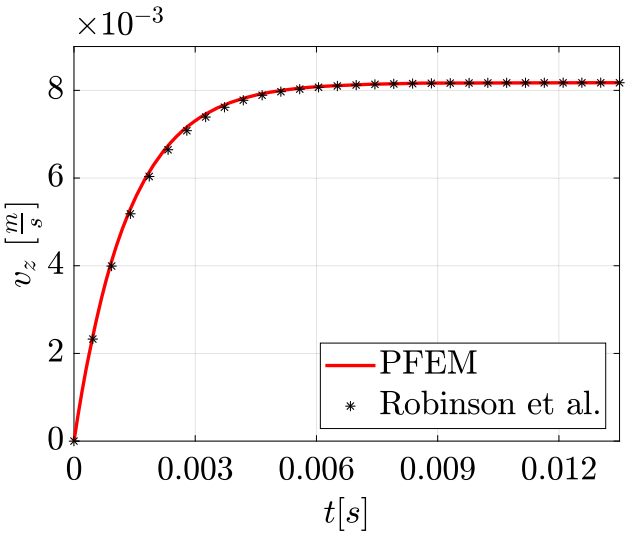

Fig. 14 Comparison the analytical z-velocity component from [52] and the present approach

number regimes and is derived using dimensional analysis based on the Buckingham theorem. The resulting expression for the drag force is presented in Eq. (A4).

$$\mathbf{F}_d = \frac{1}{2}\rho_f C_d \pi \left(\frac{d_p}{4}\right)^2 |\mathbf{u} - \mathbf{v}|\,(\mathbf{u} - \mathbf{v}) \tag{A4}$$

where $\mathbf{u}$ is the fluid velocity and C_d is the drag coefficient. The drag coefficient C_d is obtained empirically. Numerous correlations and extrapolations for C_d exist in the literature [53]. In this work, the relation proposed by [53] (Eq. A5) has been adopted, as it is one of the most comprehensive formulations and accounts for the influence of particle shape through the sphericity coefficient.

$$C_d = \frac{24}{Re_p}\left(1 + A^* Re_p^{B^*}\right) + \frac{C^*}{1 + \frac{D^*}{Re_p}} \tag{A5}$$

where A^*, B^*, C^*, D^* are empirical expressions depending of the shape of the particle, $Re_p = \frac{\rho_f \|\mathbf{v}\|_2 d_p}{\mu}$ is the particle Reynolds number and $\|\bullet\|_2$ is the euclidean norm.

The results for the two densities of $\rho_f = 1125\frac{kg}{m^3}$ and $\rho_f = 1500\frac{kg}{m^3}$ are presented in Fig. 15. After a transient phase, the particle reaches a steady-state configuration resulting from the balance of the forces acting on it. Consequently, the values used for the falling velocity parameter in the example of Section 5.3 are equal to the value reached at steady-state condition, meaning $w_{s0} = 0.2746\frac{m}{s}$ for $\rho_f = 1500\frac{kg}{m^3}$ and $w_{s0} = 0.1221\frac{m}{s}$ for $\rho_f = 1125\frac{kg}{m^3}$.

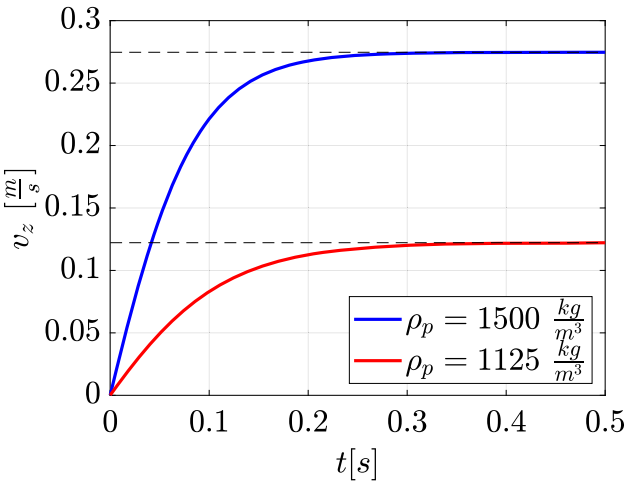

Fig. 15 z-velocity component of velocity related to the falling particle velocity of section 5.3

Acknowledgements This research was partially supported by the Italian Ministry of University and Research through the project PRIN2022 DTWIX: development of Digital TWIns for multiphysics simulation of eXtreme events in civil engineering (PRIN DTWIX - 2022AL5MSN) and by ICSC—Centro Nazionale di Ricerca in High Performance Computing, Big Data, and Quantum Computing funded by European Union—NextGenerationEU.

Funding Open access funding provided by Politecnico di Milano within the CRUI-CARE Agreement.

Data Availability Data will be made available on reasonable request.

Declarations

Conflict of interest The authors declare no potential conflict of interest.

References

1. Barnes C, Faranda D, Coppola E, Grazzini F, Zachariah M, Lu C, Kimutai J, Pinto I, Pereira C, Sengupta S et al. (2023) Limited net role for climate change in heavy spring rainfall in Emilia-Romagna. 99:56789 https://doi.org/10.25561/104550
2. Donnini M, Santangelo M, Gariano SL, Bucci F, Peruccacci S, Alvioli M, Althuwaynee O, Ardizzone F, Bianchi C, Bornaetxea T, Brunetti MT, Cardinali M, Esposito G, Grita S, Marchesini I, Melillo M, Salvati P, Yazdani M, Fiorucci F (2023) Landslides triggered by an extraordinary rainfall event in Central Italy on September 15, 2022. Landslides 20(10):2199–2211. https://doi.org/10.1007/s10346-023-02109-4
3. Messa GV, Malin M, Malavasi S (2014) Numerical prediction of fully-suspended slurry flow in horizontal pipes. Powder Technol 256:61–70. https://doi.org/10.1016/j.powtec.2014.02.005
4. Capecelatro J, Desjardins O (2013) Eulerian–Lagrangian modeling of turbulent liquid-solid slurries in horizontal pipes. Int J Multiph Flow 55:64–79. https://doi.org/10.1016/j.ijmultiphaseflow.2013.04.006
5. Iverson RM (1997) The physics of debris flows. Rev Geophys 35(3):245–296. https://doi.org/10.1029/97RG00426
6. Chang H, Chen A, Ma R, Ge B (2024) Eulerian consistent smoothed particle hydrodynamics (SPH) method for weakly compressible viscous flows applied to lid-driven cavity. Comput Part Mech 11(2):643–656. https://doi.org/10.1007/s40571-023-00644-4
7. Idelsohn SR, Oñate E, Pin FD (2004) The particle finite element method: a powerful tool to solve incompressible flows with free-surfaces and breaking waves. Int J Numer Meth Eng 61(7):964–989. https://doi.org/10.1002/nme.1096
8. Cremonesi M, Franci A, Idelsohn S, Oñate E (2020) A state of the art review of the particle finite element method (PFEM). Arch Comput Methods Eng 27(5):1709–1735. https://doi.org/10.1007/s11831-020-09468-4
9. Franci A, Cremonesi M (2017) On the effect of standard PFEM remeshing on volume conservation in free-surface fluid flow problems. Comput Part Mech 4(3):331–343. https://doi.org/10.1007/s40571-016-0124-5
10. Franci A, Zhang X (2018) 3D numerical simulation of free-surface Bingham fluids interacting with structures using the PFEM. J Non-Newton Fluid Mech 259:1–15. https://doi.org/10.1016/j.jnnfm.2018.05.001
11. Zhu M, Scott MH (2022) A PFEM background mesh for simulating fluid and frame structure interaction. J Struct Eng 148(6):04022051. https://doi.org/10.1061/(ASCE)ST.1943-541X.0003334
12. Rodríguez JM, Carbonell JM, Cante JC, Oliver J (2017) Continuous chip formation in metal cutting processes using the Particle Finite Element Method (PFEM). Int J Solids Struct 120:81–102. https://doi.org/10.1016/j.ijsolstr.2017.04.030
13. Zhang D, Rodriguez JM, Ye X, Müller R (2023) A particle finite element method for additive manufacturing simulations. J Comput Inf Sci Eng 23(5):051008. https://doi.org/10.1115/1.4062143
14. Schewe M, Noll I, Bartel T, Menzel A (2025) Towards the simulation of metal deposition with the particle finite element method and a phase transformation model. Comput Methods Appl Mech Eng 437:117730. https://doi.org/10.1016/j.cma.2025.117730
15. Février S, Fernández E, Lacroix M, Boman R, Ponthot J-P (2025) Simulation of melt pool dynamics including vaporization using the particle finite element method. Comput Mech 75(6):1787–1815. https://doi.org/10.1007/s00466-024-02571-4
16. Rodriguez JM, Carbonell JM, Cante JC, Oliver J (2016) The particle finite element method (PFEM) in thermo-mechanical problems. Int J Numer Meth Eng 107(9):733–785. https://doi.org/10.1002/nme.5186
17. Franci A, Oñate E, Carbonell JM, Chiumenti M (2017) PFEM formulation for thermo-coupled FSI analysis. Application to nuclear core melt accident. Comput Methods Appl Mech Eng 325:711–732. https://doi.org/10.1016/j.cma.2017.07.028
18. Galano N, Moreno-Casas PA, Abell JA (2021) Extending the particle finite element method for sediment transport simulation. Comput Methods Appl Mech Eng 380:113772. https://doi.org/10.1016/j.cma.2021.113772
19. Oñate E, Celigueta MA, Latorre S, Casas G, Rossi R, Rojek J (2014) Lagrangian analysis of multiscale particulate flows with the particle

finite element method. Comput Part Mech 1(1):85–102. https://doi.org/10.1007/s40571-014-0012-9
20. Franci A, de Pouplana I, Casas G, Celigueta MÁ, González-Usúa J, Oñate E (2020) PFEM-DEM for particle-laden flows with free surface. Comput Part Mech 7(1):101–120. https://doi.org/10.1007/s40571-019-00244-1
21. Cremonesi M, Ferri F, Perego U (2017) A basal slip model for Lagrangian finite element simulations of 3D landslides. Int J Numer Anal Meth Geomech 41(1):30–53. https://doi.org/10.1002/nag.2544
22. Rizzieri G, Ferrara L, Cremonesi M (2024) Simulation of viscoelastic free-surface flows with the particle finite element method. Comput Part Mech 11(5):2043–2067. https://doi.org/10.1007/s40571-024-00730-1
23. Rizzieri G, Ferrara L, Cremonesi M (2024) Numerical simulation of the extrusion and layer deposition processes in 3D concrete printing with the Particle Finite Element Method. Comput Mech 73(2):277–295. https://doi.org/10.1007/s00466-023-02367-y
24. Franci A, Cremonesi M, Perego U, Crosta G, Oñate E (2020) 3D simulation of Vajont disaster. Part 1: numerical formulation and validation. Eng Geol 279:105854. https://doi.org/10.1016/j.enggeo.2020.105854
25. Shashi Menon E (2011) Chapter 1 - design basis. In: Menon ES (ed) Pipeline planning and construction field manual. Gulf Professional Publishing, Boston, pp 1–41. https://doi.org/10.1016/B978-0-12-383867-4.00001-3
26. Messa GV, Matoušek V (2020) Analysis and discussion of two fluid modelling of pipe flow of fully suspended slurry. Powder Technol 360:747–768. https://doi.org/10.1016/j.powtec.2019.09.017
27. Richardson JF, Zaki WN (1997) Sedimentation and fluidisation: Part I. Chem Eng Res Des 75:82–100. https://doi.org/10.1016/S0263-8762(97)80006-8
28. Bombardelli FA, Jha SK (2009) Hierarchical modeling of the dilute transport of suspended sediment in open channels. Environ Fluid Mech 9(2):207–235. https://doi.org/10.1007/s10652-008-9091-6
29. Thomas DG (1965) Transport characteristics of suspension: Viii. A note on the viscosity of Newtonian suspensions of uniform spherical particles. J Colloid Sci 20(3):267–277. https://doi.org/10.1016/0095-8522(65)90016-4
30. Poletto M, Joseph D (1995) Effective density and viscosity of a suspension. J Rheol-J RHEOL 39:323–343. https://doi.org/10.1122/1.550692
31. Coussot P (1995) Structural similarity and transition from newtonian to non-newtonian behavior for clay-water suspensions. Phys Rev Lett 74:3971–3974. https://doi.org/10.1103/PhysRevLett.74.3971
32. Dohrmann CR, Bochev PB (2004) A stabilized finite element method for the stokes problem based on polynomial pressure projections. Int J Numer Meth Fluids 46(2):183–201. https://doi.org/10.1002/fld.752
33. Quarteroni A (2014) Numerical Models for Differential Problems, vol 8, 2nd edn. Springer, Milan. https://doi.org/10.1007/978-88-470-5522-3
34. Cremonesi M, Meduri S, Perego U (2020) Lagrangian-Eulerian enforcement of non-homogeneous boundary conditions in the Particle Finite Element Method. Comput Part Mech 7(1):41–56. https://doi.org/10.1007/s40571-019-00245-0
35. Cheng KJ (1984) Bottom-boundary condition for nonequilibrium transport of sediment. J Geophys Res Ocean 89(C5):8209–8214. https://doi.org/10.1029/JC089iC05p08209
36. Tezduyar TE (1991) Stabilized finite element formulations for incompressible flow computations. Adv Appl Mech 28:1–44. https://doi.org/10.1016/S0065-2156(08)70153-4
37. Si H (2015) TetGen, a delaunay-based quality tetrahedral mesh generator. ACM Trans Math Softw 41(2):1–36. https://doi.org/10.1145/2629697
38. Meduri S, Cremonesi M, Perego U (2019) An efficient runtime mesh smoothing technique for 3D explicit Lagrangian free-surface fluid flow simulations. Int J Numer Meth Eng 117(4):430–452. https://doi.org/10.1002/nme.5962
39. Fu C, Cremonesi M, Perego U, Hudobivnik B, Wriggers P (2025) Particle Virtual Element Method (PVEM): an agglomeration technique for mesh optimization in explicit Lagrangian free-surface fluid modelling. Comput Methods Appl Mech Eng 433:117461. https://doi.org/10.1016/j.cma.2024.117461
40. Edelsbrunner H, Mücke EP (1994) Three-dimensional alpha shapes. ACM Trans Graph 13(1):43–72. https://doi.org/10.1145/174462.156635
41. Fernández E, Février S, Lacroix M, Boman R, Papeleux L, Ponthot J-P (2023) A particle finite element method based on level-set functions. J Comput Phys 487:112187. https://doi.org/10.1016/j.jcp.2023.112187
42. Cerquaglia ML, Deliége G, Boman R, Terrapon V, Ponthot J-P (2016) Free-slip boundary conditions for simulating free-surface incompressible flows through the particle finite element method. Int J Numer Methods Eng. https://doi.org/10.1002/nme.5439
43. Hsu H-C, Torres-Freyermuth A, Hsu T-J, Hwung H-H, Kuo P-C (2014) On dam-break wave propagation and its implication to sediment erosion. J Hydraul Res 52(2):205–218. https://doi.org/10.1080/00221686.2013.857365
44. Liu X, Nayamatullah M (2014) Semianalytical solutions for one-dimensional unsteady nonequilibrium suspended sediment transport in channels with arbitrary eddy viscosity distributions and realistic boundary conditions. J Hydraul Eng 140(5):04014011. https://doi.org/10.1061/(ASCE)HY.1943-7900.0000874
45. Jobson HE, Sayre WW (1970) Vertical transfer in open channel flow. J Hydraul Div 96(3):703–724. https://doi.org/10.1061/JYCEAJ.0002374
46. Kumbhakar M, Mohan S, Ghoshal K, Kumar J, Singh VP (2022) Semianalytical solution for nonequilibrium suspended sediment transport in open channels with concentration-dependent settling velocity. J Hydrol Eng 27(2):04021048. https://doi.org/10.1061/(ASCE)HE.1943-5584.0002160
47. Liu X (2016) Analytical solutions for steady two-dimensional suspended sediment transport in channels with arbitrary advection velocity and eddy diffusivity distributions. J Hydraul Res 54(4):389–398. https://doi.org/10.1080/00221686.2016.1168880
48. Mehta AP, Sutherland BR, Kyba PJ (2002) Interfacial gravity currents. II. Wave excitation. Phys Fluids 14(10):3558–3569. https://doi.org/10.1063/1.1503355
49. Sutherland BR, Kyba PJ, Flynn MR (2004) Intrusive gravity currents in two-layer fluids. J Fluid Mech 514:327–353. https://doi.org/10.1017/S0022112004000394
50. Lai YG, Wu K (2019) A three-dimensional flow and sediment transport model for free-surface open channel flows on unstructured flexible meshes. Fluids 4(1):18. https://doi.org/10.3390/fluids4010018
51. Aly AM, Asai M (2018) Water entry of decelerating spheres simulations using improved ISPH method. J Hydrodyn 30(6):1120–1133. https://doi.org/10.1007/s42241-018-0133-3
52. Robinson M, Ramaioli M, Luding S (2014) Fluid-particle flow simulations using two-way-coupled mesoscale SPH-DEM and validation. Int J Multiph Flow 59:121–134. https://doi.org/10.1016/j.ijmultiphaseflow.2013.11.003
53. Haider A, Levenspiel O (1989) Drag coefficient and terminal velocity of spherical and nonspherical particles. Powder Technol 58(1):63–70. https://doi.org/10.1016/0032-5910(89)80008-7